University of Alberta

Photothermal Cantilever Deflection Spectroscopy of Physisorbed Naphtha

by

Mehrdad Bagheri

A thesis submitted to the Faculty of Graduate Studies and Research
in partial fulfillment of the requirements for the degree of

Master of Science
in
Chemical Engineering

Department of Chemical and Materials Engineering

Fall 2012
Edmonton, Alberta

To my Mom, Dad and Brother

Thanks for everything

Abstract

We have used photothermal cantilever deflection spectroscopy (PCDS) for selective and sensitive detection of hydrocarbons with a particular emphasis on monitoring naphtha physisorbed on cantilevers. In PCDS, molecules physisorbed on a bi-material microcantilever are illuminated with a mid-infrared light from a monochromator. Here, we report on detecting and molecularly discriminating nanogram quantities of hydrocarbons on the cantilever using PCDS technique. The obtained PCDS and traditional IR spectroscopies results are in excellent concurrence.

We also developed a technique to determine the effective convection heat transfer (h) for the microcantilevers used in our PCDS experiments by measuring the bending of the cantilever in response to the variations of the cantilever base temperature T_b. The designed experiment is straightforward and accurate. This yields a value of 1350-1650 $W/k.m^2$. We point out that the thermal sensitivity and the optimum thickness ratio of bi-material cantilevers used in PCDS setups depends on h.

Acknowledgements

Special thanks to Professor Thundat, I really appreciate his help and support during this project. This work has been done under his supervision. I would like to thank all my colleagues. They helped me so friendly particularly Eric Hawk, Lana Norman, Amin Valiei, Inseok Chae, Charles Van Neste, and Sam Kim.

This work is supported by Canada Excellence Research Chairs (CERC) Program. We also thank COSI for partial support. We thank Oil Sands and Coal Interfacial Engineering Facility (OSCIEF), Nano Fabrication Facility, Alberta Centre for Surface Engineering & Sciences (ACSES) research facility.

Table of Content

Table of Content

List of Tables

List of figures

List of figures

List of figures

1 Introduction

1.1 Project goal

Hydrocarbons are defined as a class of organic chemical compounds composed of only carbon (C) and hydrogen (H) atoms. They consistently serve as fuels and lubricants as well as raw materials for the production of plastics, fibres, rubbers, solvents, explosives, and industrial chemicals [1]. Moreover, hydrocarbons are the principal constituents of petroleum and natural gas. In oil sands, which is composed of a mixture of sand, clay, bitumen, and water, the oil extraction process involves the routinely use of naphtha as a diluent where bitumen attached to sand particles is separated for upgrading [2].

The extraction process aim is to separate bitumen from oil sands using hot water and solvents. The extraction of bitumen from the conditioned ore slurry consists of two main steps. Separation of bitumen froth (60% bitumen, 30% water and 10% fine solids) in the primary separation vessel. The second process is diluted froth treatment in the froth tank to recover the bitumen and reject as much residual water and solids as possible. The diluted froth treatment uses either naphtha or a paraffinic solvent to cause the solids to easily settle. After processing, the oil is sold as raw bitumen or upgraded and then sold as synthetic crude oil in the oil market [2].

Naphtha, a complex mixture of hydrocarbons, is a very valuable product of crude oil. The froth treatment tailings have residual solvent associated with them. Therefore, they are passed through a diluent stripper before discharge into tailings pond. Even after naphtha recovery process, less than one percent of naphtha loss to tailing streams is inevitable in the oil sands extraction process. Naphtha as a food source for microorganism causes microbial contaminations resulting in turbidity, corrosion and increasing in maintenance cost of pipelines [3]. Presently, naphtha concentrations are monitored by manually collecting samples at 6 hour intervals and then the samples are transported to a laboratory for analysis by gas chromatography-mass spectrometer, which is a bulky and expensive technique that often requires a trained operator [2]. Therefore, there is a need to develop a portable on-site detection device for targeted hydrocarbons that is selective, sensitive, and quantitative with real-time detection capabilities. In addition, the detection of hydrocarbons, which include thousands of different molecules, would enable us to have a better PCDS peaks identification of an unknown mixture, which is the most realistic situation in naturally occurring systems.

1.2 Nano & Microcantilevers

In 1986, Gerber et al. invented atomic force microscope (AFM) using a micro-size cantilever [4]. Basically, the AFM functions as a miniaturized phonograph where images are obtained by raster scanning the surface with an

AFM probe. The probe includes a sharp tip mounted on a microcantilever, which deflects due to the forces between tip and sample [4, 5]. Typically, there are two shapes for cantilevers: rectangular and V-shaped (shown Figure 1.1) which are of the order of 100-1000 μm long, 30-100 μm width and 0.5-1 μm thickness. Nano and microcantilevers mostly are made of silicon or silicon nitride and are manufactured by a technique which is called microfabrication. Microfabrication is an engineering development that allows the construction of structures with well-controlled micron-scaled features [6].

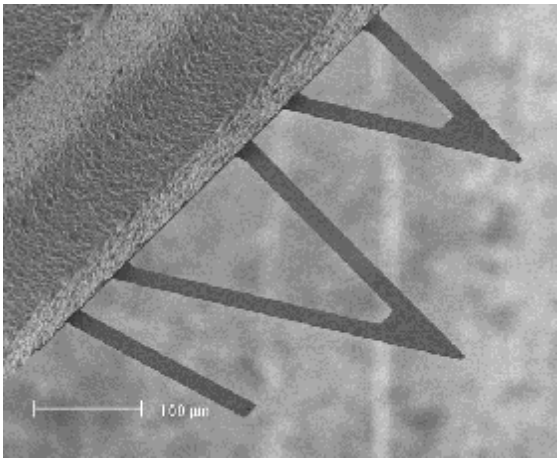

Figure 1.1 V-shaped and rectangular microcantilevers

1.3 Cantilever sensors

The same microcantilevers that are used in scanning probe microscopy techniques have garnered considerable interest as potential sensing devices [4, 7]. Thomas Thundat and co-workers demonstrated ability of microcantilevers sensors to detect chemisorbed or physisorbed adsorbates. These miniature sensors, such as microfabricated cantilever array systems, exhibit high

sensitivity for detecting molecular adsorption at picogram levels. [8, 9]. The sensitivity is defined cantilever defection response regarding to temperature or mass changes.

Generally, molecules detection by microcantilevers sensors is classified two main groups; labeled and label-free methods. Labeled sensors have high sensitivity and large dynamic range of spatial resolution; they also have drawbacks such as time required for extensive sample preparation leading to significant delay in identification. It also requires high cost and skilled scientists for labeling processes and detecting systems. Alternative methods to substitute labeling techniques are label-free methods. Rapid and real-time detections are primary advantages of label-free methods [10].

The Microcantilevers work in three basic modes: bi-material, dynamic and surface stress modes. In bi-material mode, microcantilevers undergo a static deflection in the response of temperature changes because of different coefficients of thermal expansion between the metallic thin film and the underlying substrate. This mode is widely used for temperature related applications such as thermal actuators. Static sensing measures the magnitude of the bending of the microcantilever beam. The cantilevers bend due to adsorption-induced stress causing by molecular adsorption. The bending carries information about the adsorbed molecule usually due to a functionalized chemical coating applied to the microcantilever surface prior to detection. Dynamic sensing absorption of molecules on cantilever surface changes the resonant frequency. Changes in resonant frequency allow inertial properties to be measured such as the mass of the adsorbed molecules [7-9].

When operated in dynamic mode the cantilevers are excited close to their resonance frequency, which is typically on the order of tens of kHz to a few MHz, where resonance frequency changes are readily observed when an additional mass is adsorbed at the oscillating cantilever interface [11]. For a rectangular cantilever, the change in mass (Δm) can be calculated from the variation in the resonance frequency by equation(1.1).

$$\Delta m = \frac{K_{spring}}{4p^2}\left(\frac{1}{f_1^2} - \frac{1}{f_0^2}\right) \tag{1.1}$$

where f_o and f_1 are the measured resonance frequency before and following molecular deposition, respectively, and k_{spring} is the cantilever spring constant [8]. However, detecting adsorbed mass does not provide any information regarding the chemical nature of the adsorbed molecules.

In order to have a selective cantilever-base sensor, cantilever surface is coated with specific sorbents adsorbing target molecules. The adsorbed molecules interaction with the medium results the resonance frequency shift or bending of cantilever. Many different sorbents have been employed to coat cantilever sensors such as thiol-based chemistry on gold-coated cantilevers [12], antibase-based functionalization [13], amine-functionalized mesoporous silica [14] and so on. Each of these operation modes are schematically represented in Figure 1.

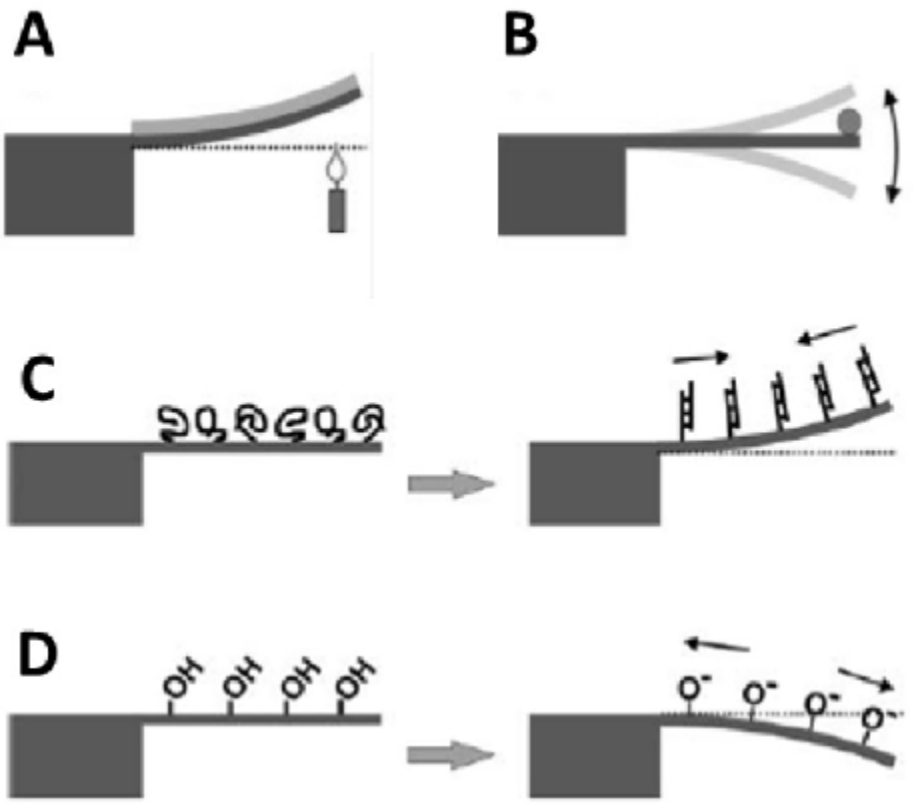

Figure 1.2. Different operation mode of microcantilever sensors. A) bi-material mode, B) dynamic mode, C) tensile surface stress (DNA hybridization [15, 16]) D) compressive surface stress.

Since reversibility is a significant characteristic for an applicable sensor, the interactions between receptors and target molecules should be weak enough to be broken in room conditions. Therefore, immobilizing chemical interfaces on the cantilever can provide only limited selectivity in complex mixtures. Moreover, detection of molecules is restricted to availability of proper receptors while in most cases finding the receptors is really challenging. Hence, in spite of the cantilever sensors high sensitivity, its applicability as a commercialized sensor is hindered by its selectivity unless a versatile method is employed by which expected selectivity can be reached.

1.4 Photothermal cantilever deflection spectroscopy

Another way of achieving high chemical selectivity corresponding to mass changes for microcantilever sensors is by combing them with spectroscopic techniques. Exciting the adsorbed molecules using infrared radiation and measuring the nonradiative decay-induced temperature changes in the cantilever via a bi-material effect offers excellent selectivity. The high temperature sensitivity of bi-material microcantilever was first introduced by Gimzewski et al. [17] where they described a new kind of calorimeter providing ability to measure about pico-joule heat produced by catalytic conversion of H_2 and O_2 to H_2O. They then combined the bi-material cantilevers with photothermal spectroscopy [18]. The bi-material cantilevers due to their micro-size and low thermal mass allow pico-gram to be analysed. In this case, the bi-material cantilever beam was demonstrated to be sensitive enough to measure power of 100 pW, energy of 150 fJ or measuring 10^{-5} K [18, 19].

Bi-material microcantilevers have excellent thermal sensitivity and undergo bending due to very small temperature changes due to the unequal thermal expansion coefficient. In the PCDS technique, physisorbed molecules on the bi-material cantilever are exposed to mid-infrared (IR) light in a sequential manner. When the IR frequency matches with the vibrational frequency of a bond, the molecule is excited into resonance. The nonradiative decay of the excited molecules results in the generation of heat which bends the bi-material cantilever. A cantilever bending plot as a function of illumination wavelength replicates an IR absorption spectra of the absorbed

molecules [19]. However, in general the static deflection of a bi-material microcantilever can be very noisy due to ambient temperature fluctuations. Therefore, a pulsed illumination source with a certain frequency is used in combination with a lock-in amplifier to monitor the cantilever motion due to the inherent bi-material effect. The pulse frequency of the IR illumination is kept at a period where heat transfer from the adsorbed analytes to the cantilever is maximized. The measured amplitude of the cantilever deflection as a function of illumination wavelength shows a nanomechanical IR absorption spectrum of the adsorbed molecules [7, 20]. Another advantage of PCDS method over traditional spectroscopy is that much smaller amounts of material (subnanogram quantities) are required in comparison with milligram quantities needed for traditional infrared spectroscopy [6, 8-10]. These advantages have loaned themselves to a very sensitive detection method which has been employed for the detection of a variety of molecules including explosive materials [21-23], DNA, and biological warfare agents for forensics and homeland security [10, 12-14].

Here, we report on the selective and sensitive detection of hydrocarbons, n-heptane and 1-octene, as well as the hydrocarbon mixture like naphtha. Since the selectivity of this method is limited by thermal sensitivity of the microcantilever, we have optimized the thickness of the gold layer deposited on the silicon cantilever. In this study, we demonstrate that the microcantilever-based PCDS technique could be a viable alternative for traditional chemicals detection methods since PCDS offers cheap, selective

and highly sensitive sensing capabilities for detection of the hydrocarbon molecules.

2 Experimental Procedure

2.1 Cantilever preparation

Commercially available silicon cantilevers (OCTOSENSIS-Micromotive GmbH, Germany) have been used in these experiments. The chips contain an array of eight cantilevers having typical dimensions of 500 µm in length, 90 µm in width, and 1.0 ± 0.3µm in thickness with a spring constant of 23 mN/m and corresponding resonance frequency of 24.3 KHz. These values are listed according to the manufacturer. Prior to vacuum deposition, all cantilevers were thoroughly cleaned in piranha solution (H_2SO_4:H_2O_2 3:1) and followed by immersing them in Milli-Q water and then ethanol 95%. In order to render the cantilevers bi-material, the cantilevers were deposited with adlayers of gold having thickness of 50, 100, 200, and 250 nm with an e-beam evaporator at rate of 0.2 Å/s. A thin layer of titanium (10 nm) served as the adhesion layer before gold deposition at rate of 0.3 Å/s. The used naphtha (petroleum ether), n-heptane 99%, and 1-octene 99% were purchased from Fisher scientific (USA) and used without further purification. The chemicals were deposited on the cantilevers by physically dipping them in the solutions for a few seconds followed by air drying.

2.2 Experimental Setup

The experimental setup is described here (Figure 2.1). The cantilevers were mounted on a stainless steel cantilever holder and then positioned in the head unit of a MultiMode atomic force microscope (AFM) (Bruker, Santa Barbara, CA). IR radiation illuminating from the monochromator is focused onto the cantilever by a concave mirror. A diode laser having a wavelength of 670 nm reflected off the cantilever beam monitored by a position sensitive detector (PSD). In this configuration, the resonance frequencies of the cantilevers were measured before and after hydrocarbon deposition with a SR760 spectrum analyser (Standford Research Systems, Sunnyvale, CA) before each run. Changes in the PSD signals arising from cantilever deflections are processed and saved by a SR850 lock-in amplifier (Stanford Research Systems, Sunnyvale, CA). IR radiation illuminating from the monochromator is focused onto the cantilever via a concave mirror. The focused light is chopped at a frequency of 80 Hz to remove ambient noise. The employed monochromator illuminates in the mid-IR range between 2.5 to 14.5 μm (i.e., 4000 cm^{-1} to 690 cm^{-1}) and the resolution is 0.05 μm at 3 μm, 0.12 μm at 6 μm, and 0.25 μm at 11 μm. The microcantilever deflection response is plotted using a Labview system and corresponds to the PCDS spectrum of the hydrocarbons adsorbed the bi-material cantilever interface.

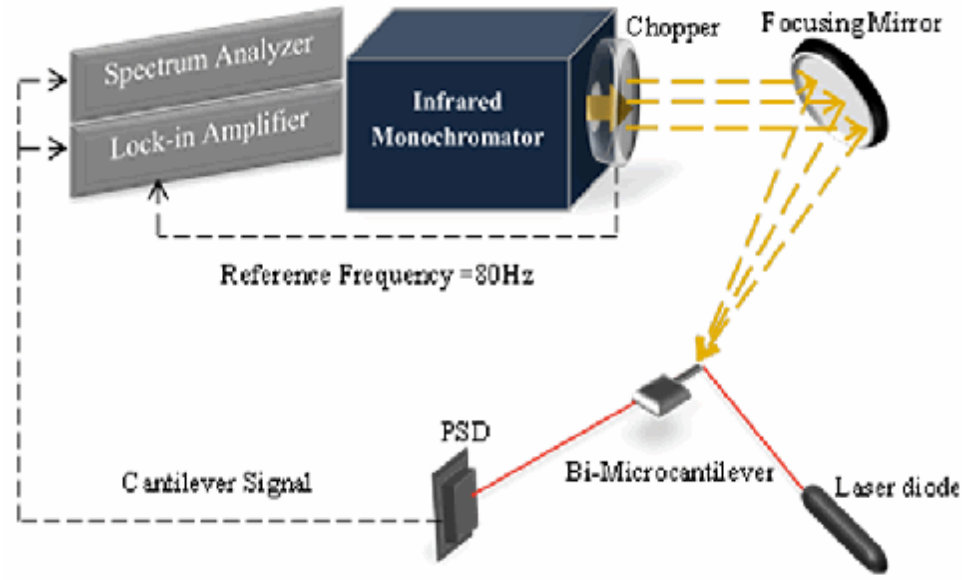

Figure 2.1 Schematic figure of the setup used for PCDS experiments. IR light from monochromator is chopped at 80 Hz and focused on the cantilever by a concave mirror. Reflections of an optical laser diode light off the cantilever on PSD are recorded by the lock-in amplifier.

2.3 Infrared Spectroscopy

IR spectroscopy is a very powerful method for the identification of functional groups. Infrared spectra in both Attenuated Total Reflectance (ATR) and grazing angle FT-IR configurations were obtained using a Fourier transform infrared (FT-IR) spectrometer (Thermo Nicolet NEXUS 670) from 4000-700 cm^{-1}. ATR spectra were acquired by using a ZnSe crystal. Grazing angle FT-IR measurements were made at an incident angle of 75º where a total of 512 scans were acquired at a resolution of 2 cm^{-1}. For reflection mode measurements, gold-coated silicon wafers having dimensions of 1 × 1 cm were prepared using the same method mentioned above for the microcantilever measurements.

The principle of FT-IR is based on the fact that bonds and groups of bonds vibrate at characteristic frequencies. A molecule that is exposed to infrared rays absorbs infrared energy at frequencies which are characteristic to that molecule. In a molecule, the differences of charges in the electric fields of its atoms produce the dipole moment of the molecule. Molecules with a dipole moment allow infrared photons to interact with the molecule causing excitation to higher vibrational states. The absorption frequency depends on the vibrational frequency of the molecules, whereas the absorption intensity depends on how effectively the infrared photon energy can be transferred to the molecule, and this depends on the change in the dipole moment that occurs as a result of molecular vibration. The greater change in dipole moment during a vibration results the higher intensity of absorption of a photon. Diatomic molecules do not have a dipole moment since the electric fields of their atoms are equal. Also, if a molecule is so symmetrical that stretching of a bond does not produce any dipole moment, then no IR peak will be found in the spectrum. During FT-IR analysis, a spot on the specimen is subjected to a modulated IR beam [24].

3 Results and discussions

3.1 Adsorbed mass

Resonance frequencies of cantilevers were measured before and after adsorption of the target material. Figure 3.1 is an optical photo of naphtha deposited on gold side of a bi-material cantilever which shows how naphtha sticks to a cantilever surface in spite of its volatility. The mass of a 250 nm gold-coated cantilever was calculated 350 ng considering the densities of the materials (i.e., Si=2328 Kg/m^{-3} and Au=19300 Kg/m^{-3} [25]) and the dimensions of the cantilever as listed by the manufacturer. The mass of adsorbed chemicals on cantilever is varied slightly in each run. Using equation(1.1) and Figure 3.2, the mass of the material adsorbed at the cantilever interface was found to be on the order of 2-4 ng. The thicknesses of adsorbed chemicals were also measured by ellipsometry method 10 ± 2 nm. The absorbed mass theoretically calculated from ellipsometry thickness is almost same with the absorbed mass measured by the resonance frequency change.

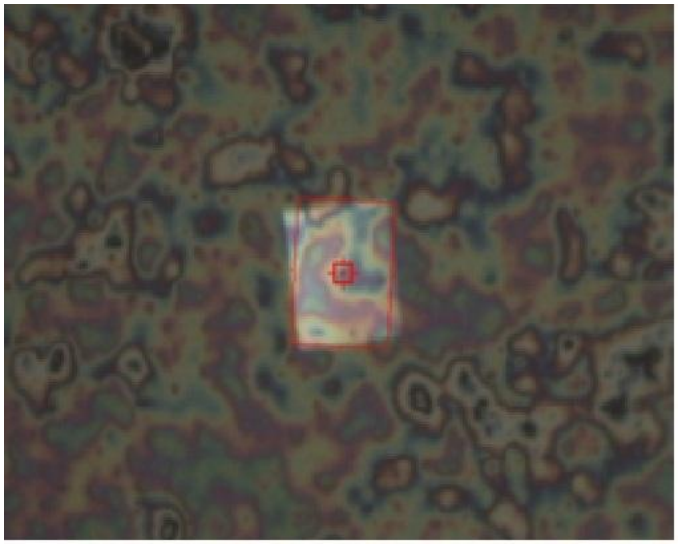

Figure 3.1. Optical image of naphtha deposited on gold side of a bi-material cantilever.

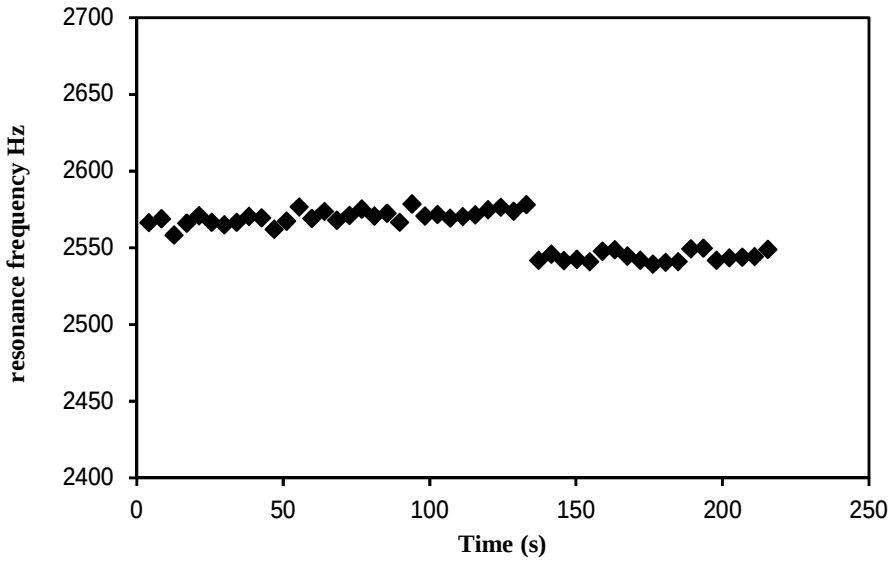

Figure 3.2. Resonance frequency shift of a 250 nm gold-coated cantilever before and after naphtha deposition.

3.2 Experiment optimization

Prior to employing the bi-material cantilever as a sensing device, a number of control and reference experiments were carried out. Using the experimental configuration illustrated in Figure 1, baseline spectra were acquired for both the bare Si and Au sides of the bi-material cantilever in the experimental spectral range of 4000-690 cm^{-1}. No apparent peaks were observed in the measured spectral range for the Au-coated side as is shown in Figure 3.3. However, two broad peaks were observed for the Si side of the cantilever. These peaks observed at 3700-2850 and 1300-900 cm^{-1} falling into the spectral region of known IR absorbance bonds for hydrocarbon molecules. Therefore, the Au-coated side of the microcantilever was chosen as the optimal surface for our sensing applications.

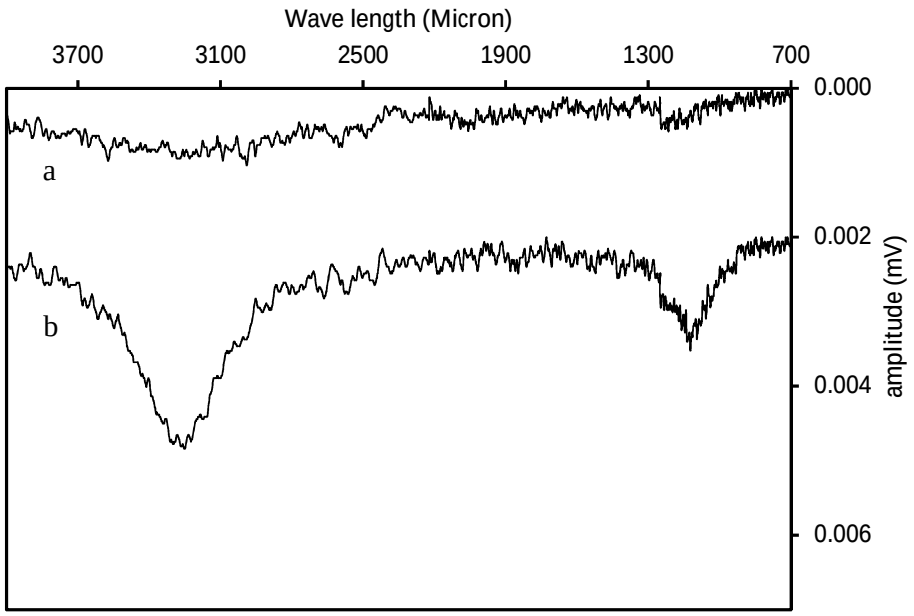

Figure 3.3. Nanomechanical IR absorption spectrum of (a) gold which is almost flat with negligible absorption peak and (b) silicon with two sharp peaks interfere in recognition of hydrocarbons peaks.

Next, it was necessary to consider the thickness of the gold adlayer. Lai et al. have shown a dependency on the cantilever response versus the thickness of the adlayer material [25]. Equation (3.1) shows the sensitivity of the sensor as a function of ratio of Au thickness over Si thickness ($n=t_1/t_2$). The sensitivity of cantilever (S) is defined deflection of tip of cantilever over incident power (p) at the end of beam.

$$S = 2[\frac{L^3}{t_2^2 w}](a_1 - a_2)[\frac{n+1}{K(l_1 n + l_2)}] \tag{3.1}$$

where

$$K = 4 + 6n + 4n^2 + (\frac{E_1}{E_2})n^3 + (\frac{E_2}{E_1})\frac{1}{n} \tag{3.2}$$

L, t, and w are the length, thickness, and width of cantilever, respectively. The subscripts 1 and 2 correspond to the gold and silicon layer, respectively. Here, E, α, λ are the elastic modulus, thermal expansion coefficient, and thermal conductivity, respectively [15]. For silicon and gold bi-material cantilever n_{opt} is calculated to be 0.32 however n=0.25 used in our experiments the sensitivity is 98% of the maximum. Figure 3.4 illustrates sensitivity of the bi-material cantilever as a function of thickness ratio of gold on silicon *n*. From equation (3.2) and experimental results (it will be shown later), it is found that the 250 nm thickness of gold on silicon microcantilever is the most sensitive. In the physical vapour deposition (PVD) process, gaseous metal atoms leaving a metal crucible surface have high temperature which in turn can cause bending of bi-material cantilever. Thus, a thick gold layer could cause huge

bending of microcantilever which makes reflection of laser off the PSD. Therefore, the cantilever with 250 nm thickness of gold was the optimum practical thickness of gold in our case.

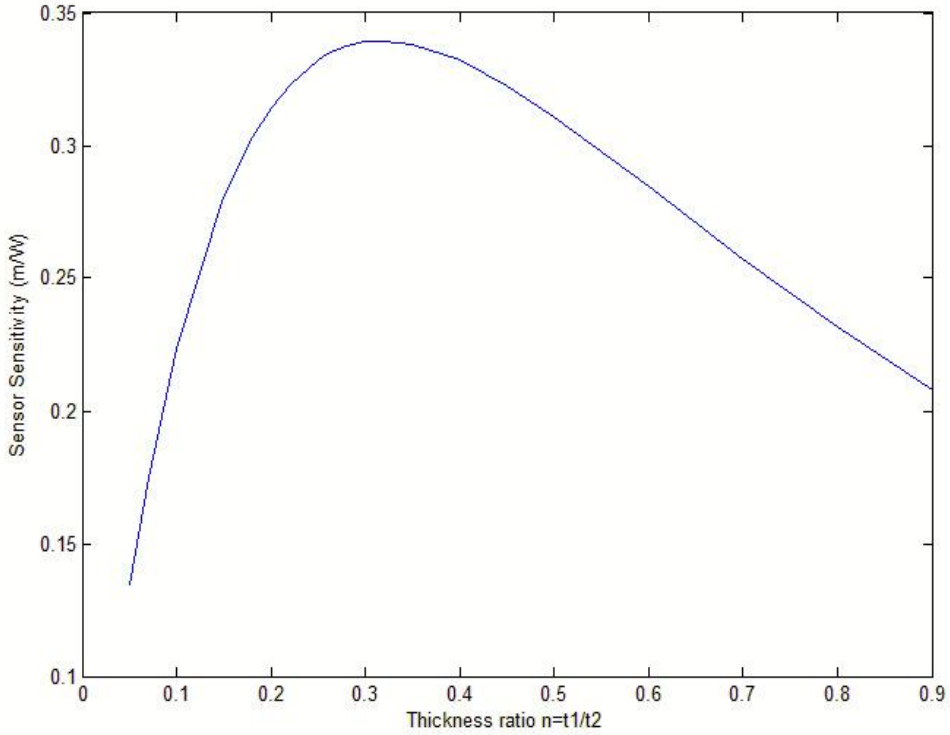

Figure 3.4. The Sensitivity of the bi-material cantilever as function of thickness ratio of gold on Si cantilever surface.

3.3 PCDS results

Many runs with different cantilevers were carried out and resulted in identical spectra. Prior to deposition of chemicals, before each experiment, a baseline IR spectrum was taken. The PCDS spectra are obtained by subtraction of IR baseline profile from chemicals nanomechanical deflections. All obtained full range spectra were the normalized to have a good qualitative comparison. Since the peaks in range of 4000-2500 cm^{-1} have high amplitude,

the weak peaks in the range of 2500-700 cm^{-1} are illustrated in a new window. The resulting naphtha peaks are in a very excellent agreement with ATR and grazing angle FT-IR spectra which are employed as references for our PCDS results as shown in Figure 3.9.

3.3.1 Naphtha

Figure 3.5 to Figure 3.8 show PCDS results for naphtha on 50, 100, 200 and 250 nm gold coated microcantilevers. Molecules absorb IR light in specific wavenumber which results molecules excitation. The excited molecules spontaneously decay to a lower lying level. The nonradiative decay transition releases phonons generating heat which is then transferred to bi-material cantilever resulting bending. Therefore, peaks amplitude in PCDS results is directly correlated with the amount of heat absorbed by a bi-material cantilever [19, 22]. There are some strong bands in naphtha spectrum corresponded to $–CH_3$ and $–CH_2–$ symmetric and anti-symmetric stretching in the range of 2990-2850 cm^{-1} which are common between all hydrocarbon molecules. From 2500-700 cm^{-1}, many peaks come into view which might be corresponded to different molecules of the mixture. The band of CH_2 scissors vibration and CH_3 anti-symmetric stretching in aliphatic compounds appears at 1475-1450 cm^{-1} and 1465-1440 cm^{-1}, respectively. In 1380-1370 cm^{-1}, symmetric deformation of CH_3 in aliphatic and in isopropyl group have a peak. Naphtha may partly contain benzene molecules which their rings shows peaks in 2000-1600 cm^{-1}. Moreover, in alkene compounds C=C double bond stretch also cause some peaks in 2000-1600 cm^{-1}. Carbon rings in cyclic

compound and =CH out of plane deformation in vinyl compound show peaks in the range of 1030-950 [26, 27].

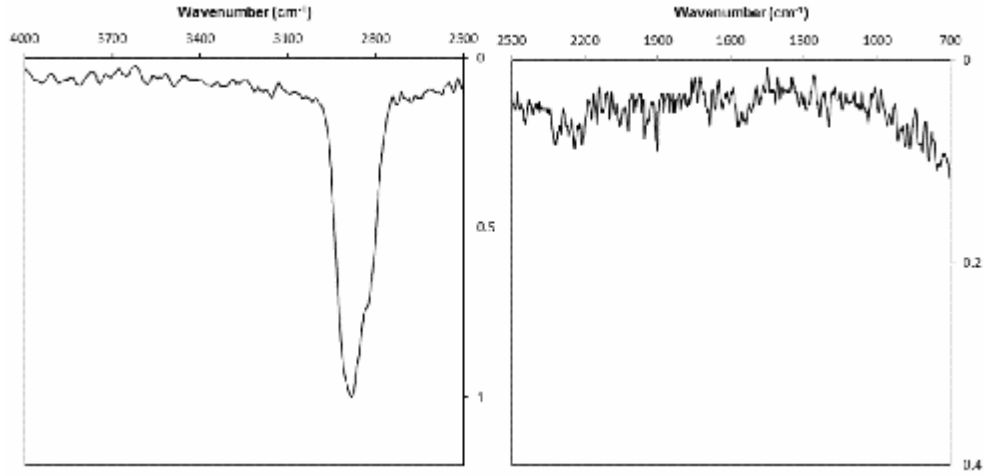

Figure 3.5. Nanomechanical deflection of bi-material 50 nm gold-coated cantilever for naphtha. The 50 nm gold-coated cantilever shows only one strong peak. No peak appeared in the range of 2500-700 cm^{-1}.

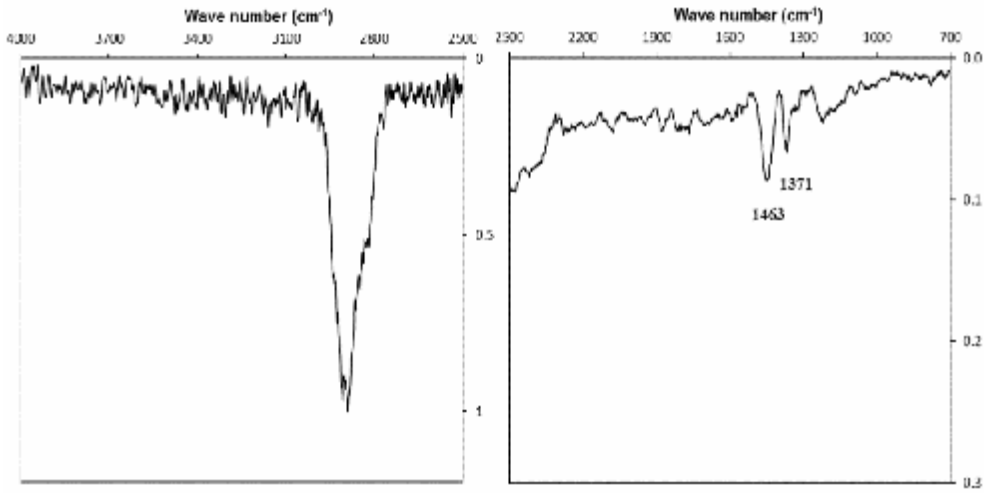

Figure 3.6. Nanomechanical deflection of bi-material 100 nm gold-coated cantilever for naphtha. In addition to the peak around 2990 cm^{-1}, two peaks are detected by increasing 50 nm gold thickness on bi-material cantilever.

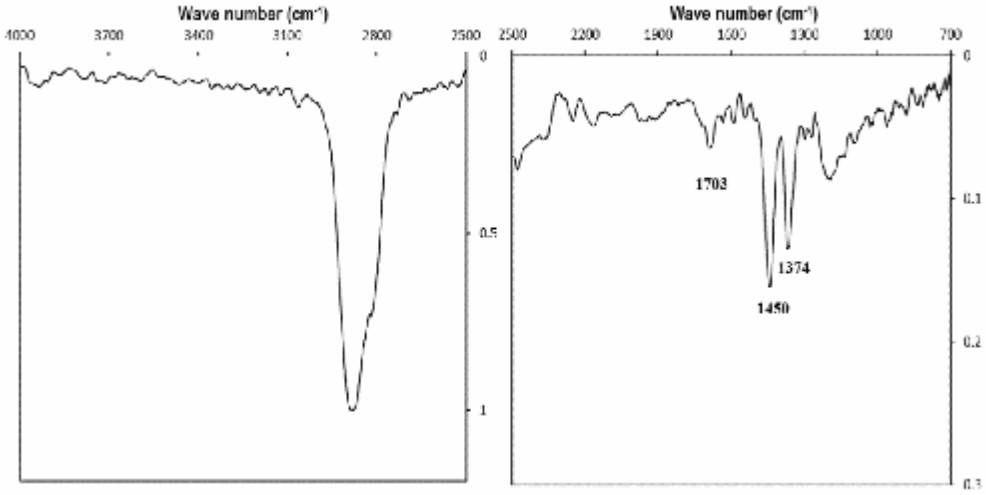

Figure 3.7. Nanomechanical deflection of bi-material 200 nm gold-coated cantilever for naphtha. The 200 nm gold-coated cantilever detects one more peak in about 1703 cm^{-1}.

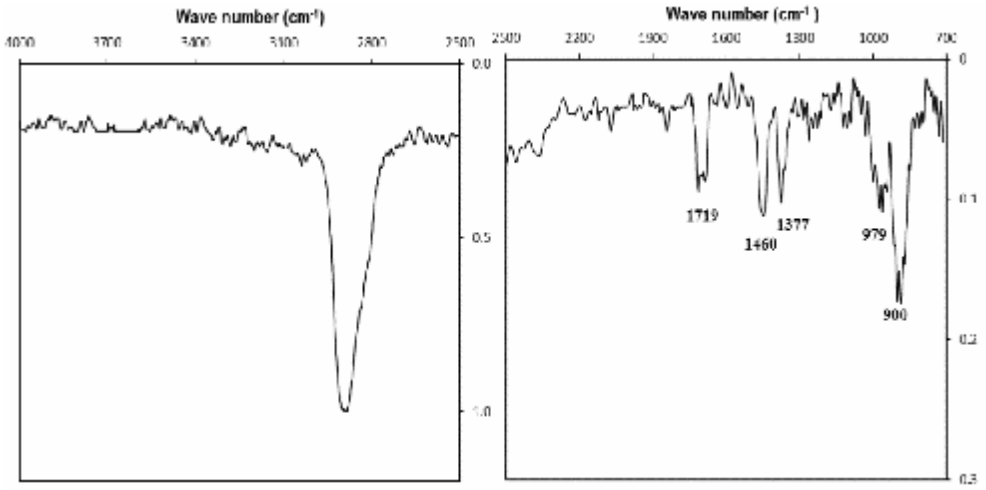

Figure 3.8. Nanomechanical deflection of bi-material 250 nm gold-coated cantilever for naphtha. The 250 nm gold-coated bi-material cantilever is enough sensitivity to show almost all peaks appearing in conventional IR spectroscopy.

As mentioned in experiment optimization (section 3.2), the bi-materials cantilevers sensitivity highly depends on thickness ratio of constitutive materials. Therefore, as thickness ratio increases the thermal sensitivity increases until it reaches a maximum amount which is 0.32 in our case according to theoretical calculations have been done. The 50, 100 nm

gold-coated cantilevers, shown in Figure 3.5 and Figure 3.6, are able to detect limited amount of peaks however recognising weak peaks is not easy due to high noise-to-signal ratio. The 200 nm gold-coated cantilever does not have enough thermal sensitivity to show all peaks while the 250 nm gold-coated cantilevers in shows all the peaks which appears in ATR and grazing angle FT-IR (Figure 3.9). The Figure 3.8 confirms that the 250 nm gold coated on 1 µm silicon cantilever is most sensitive thickness of gold which was already predicted theoretically by equation(3.1).

There are a few peaks with different intensity in comparison with conventional IR spectra. The amplitude of peaks in PCDS methods is directly proportional to the efficiency of nonradiative decay of the excited molecules which produces phonons. The thermal energy from phonons is then transferred to the bi-material sensor surface causing cantilever bending [22, 28, 29]. The resulting naphtha peaks show a very excellent agreement between PCDS and reference IR spectra with a slight shift causing by low resolution of monochromator and thermal sensitivity of microcantilevers.

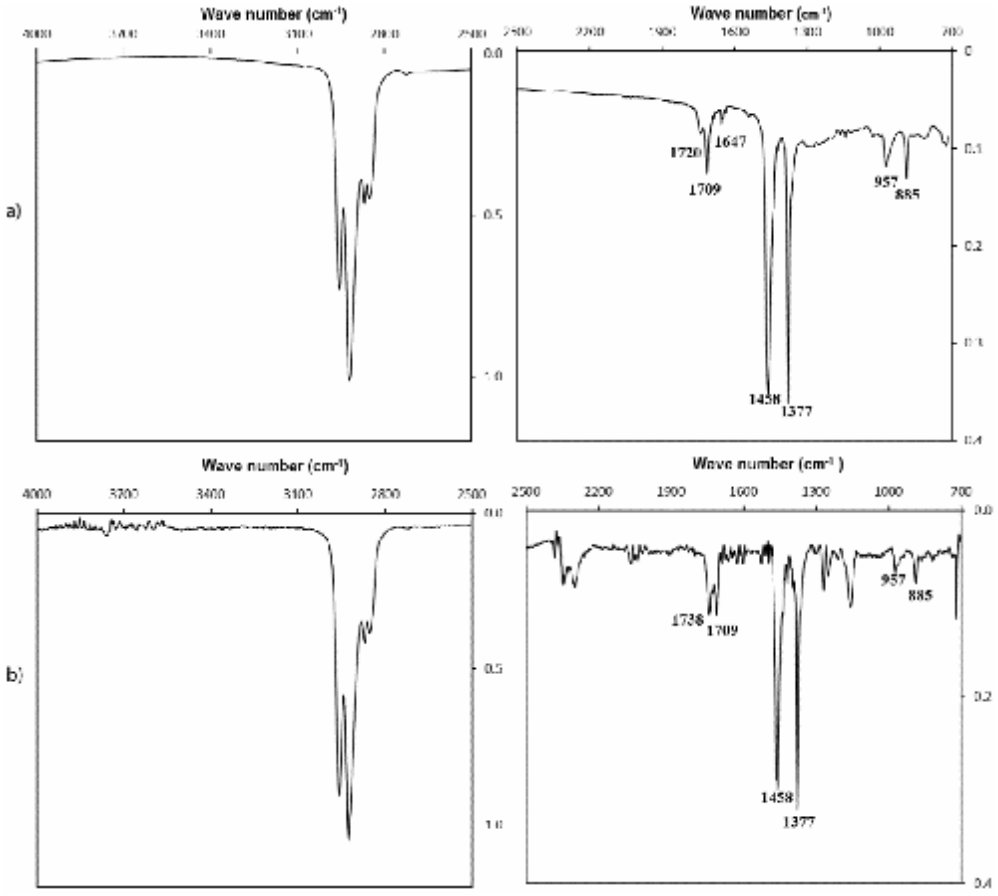

Figure 3.9. Naphtha conventional IR spectroscopy. (a) ATR spectrum of naphtha. (b) Grazing angle specular reflection FT-IR spectrum of naphtha.

3.3.2 n-heptane

As naphtha consists predominantly of a mixture of alkanes and alkenes, n-heptane and 1-octene have been also selected in order to validate the results [30]. Moreover, it provides a better knowledge of peaks appeared in naphtha spectra since numerous commercial sensors are based on this prior known knowledge. The alkane, like heptane (C_7H_{16}) gives an IR spectrum that has relatively few bands (Figure 3.10). The CH_2 scissors vibration and CH_3 anti-symmetric stretching in aliphatic compounds have peaks at 1475-1450

cm^{-1} and 1465-1440 cm^{-1}, respectively. The symmetric deformation of CH_3 in aliphatic molecules causes a peak in 1380-1370 cm^{-1}. All shown n-heptane peaks which appear in reference IR spectra (Figure 3.10) are also detected by PCDS (Figure 3.8) with a little shift.

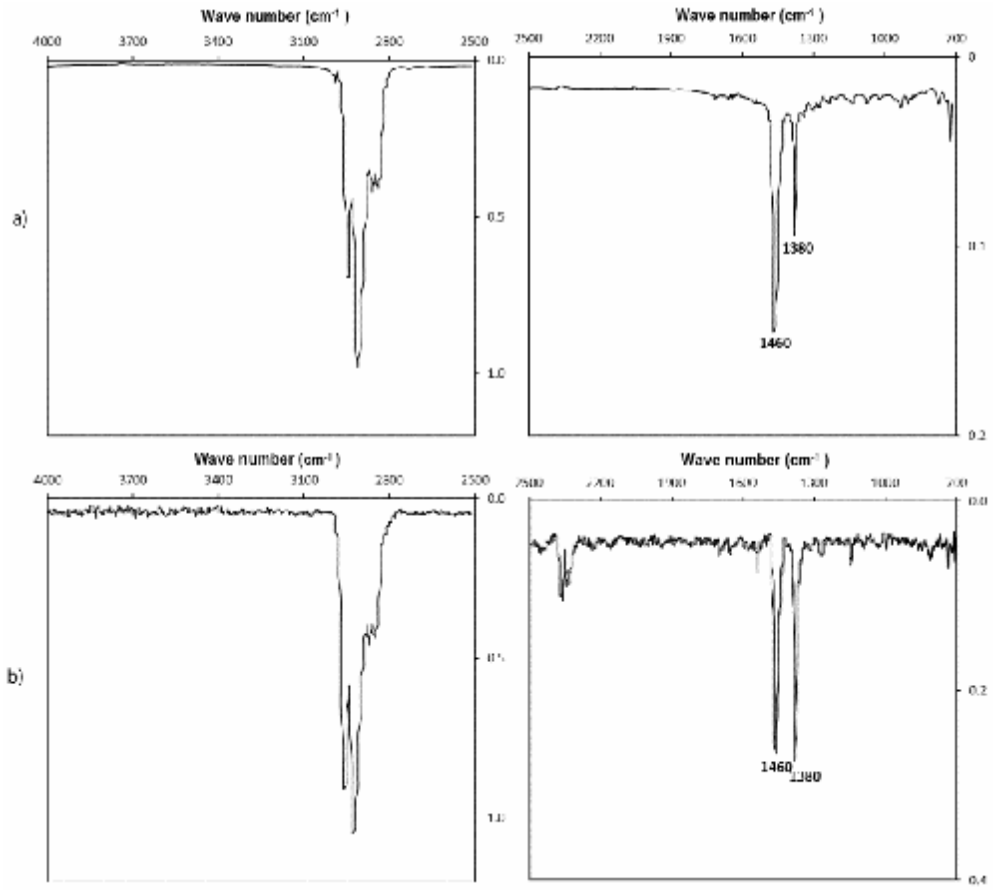

Figure 3.10. n-heptane conventional IR spectroscopy (a) ATR spectrum of n-heptane (b) grazing angle specular reflection FT-IR spectrum of n-heptane. The peaks appeared about 2400 cm^{-1} at reflection FT-IR spectra are related to CO_2.

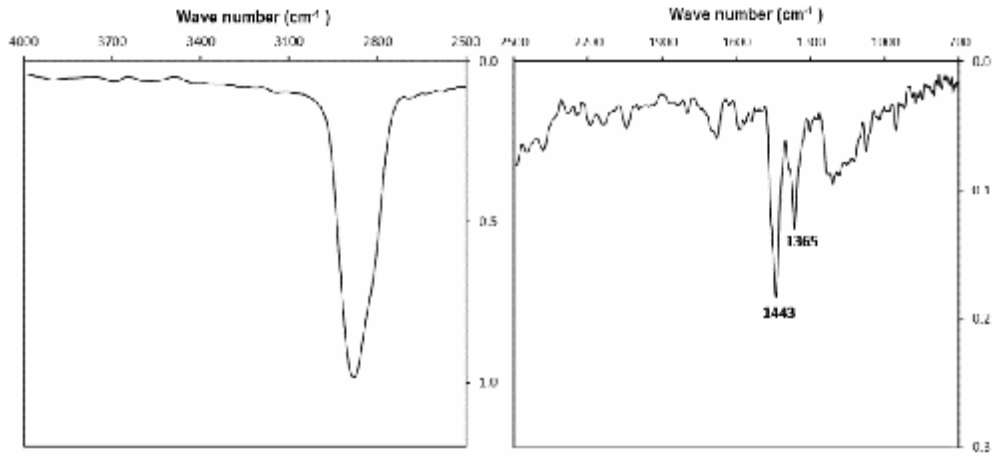

Figure 3.11. Nanomechanical deflection of bi-material 250 nm gold-coated cantilever for naphtha. The PCDS results show all peaks related to n-heptane.

The spectrum for the alkenes such as 1-octene, C_8H_{16}, has also some strong absorption bands shown in Figure 3.12. In addition to the band of CH_2 scissors vibration, CH3 anti-symmetric stretching and CH3 symmetric deformation, there is also an alkene C=C double bond stretch in the range of 1680-1630 cm^{-1} which distinguishes it from alkanes, same weak peak appeared in PCDS spectrum as is illustrated in Figure 3.13. The ATR spectrum shows out-of-plane C-H bonds for the alkene in the range 1000-900 cm^{-1} [17]. There are a few discrepancies between ATR and grazing angle specular reflection FT-IR coming from differences of these two techniques. The peaks appearing in the range of 2500-2200 cm^{-1} are corresponded to CO_2 contaminations.

3.3.3 1-octene

However, the microcantilever sensor is not capable to show all the peaks, the result of 1-ocetene is absolutely comparable with conventional IR spectra. Regarding to Figure 3.11 and Figure 3.13, PCDS provides a unique

nanomechanical deflection spectrum for alkenes and alkanes. Moreover, discrimination of alkenes and alkanes in a complex mixture such as naphtha by PCDS is possible.

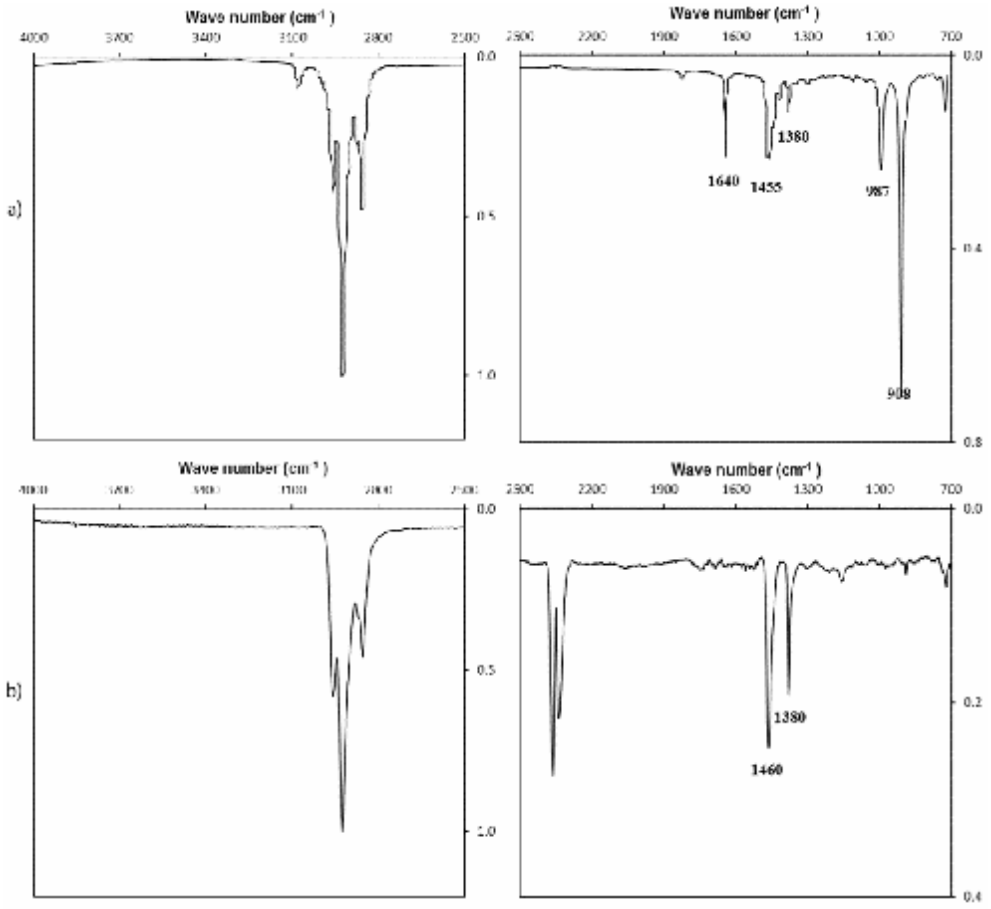

Figure 3.12. 1-octene conventional IR spectroscopy (a) ATR spectrum of 1-octene (b) Grazing angle specular reflection FT-IR spectrum of 1-octene.

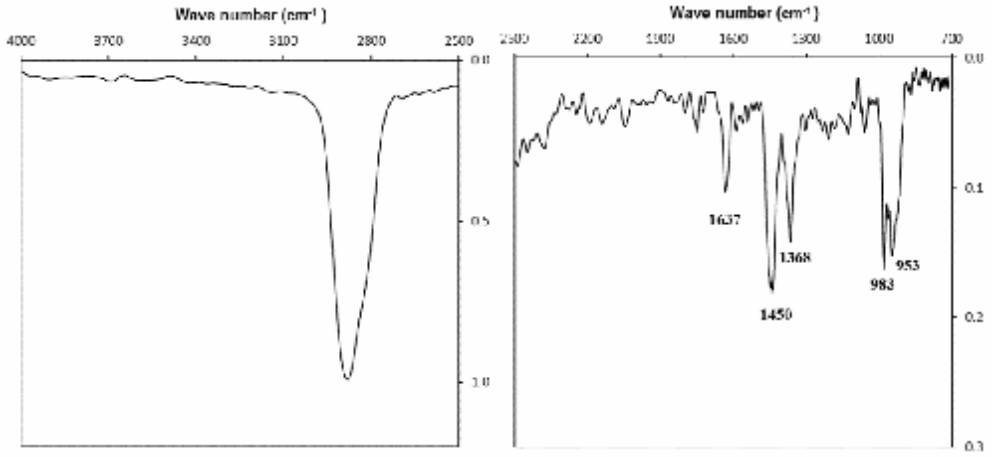

Figure 3.13. Nanomechanical deflection of the bi-material 250 nm gold-coated cantilever for 1-octene.

4 Conclusion

We have detected hydrocarbons such as naphtha, n-heptane and 1-octene with very high selectivity and sensitivity using PCDS and an optimized bi-material microcantilever. The bi-material cantilever with physisorbed hydrocarbons undergo bending when exposed to mid-infrared light in a sequential fashion. The amount material adsorbed on the cantilever is determined from the resonance frequency shift with and without adsorbents. Compared to conventional cantilever sensor technology, the advantage of the PCDS technique includes high selectivity without using any chemically selective coatings immobilized on the cantilever surface. In addition, using PCDS it is possible to obtain IR spectrum of materials in nanogram quantities compared to milligram needed in the conventional spectroscopy techniques.

5 Heat transfer of bi-material cantilevers

5.1 Introduction

5.1.1 Overview

As discussed in the previous chapters, besides using cantilevers in the AFM, bi-material cantilevers have an enormous potential to detect temperature change as small as 10^{-5} K due to its miniature dimensions and thermal mass [18, 19]. Bi-material cantilevers were first used as a chemical reaction calorimeter where heat generated by the catalytic reaction of H and O on a Platinum catalyst was measured [18]. Afterwards, photothermal cantilever deflection spectroscopy (PCDS) was developed in order to detect an arbitrary material adsorbed on a bi-material cantilever surface using mid-IR light [19, 22, 31].

More recently, a novel sensitive method has been introduced using a microsphere attached to a bi-material microcantilever to measure near-field radiative heat transfer between the microsphere and a flat substrate by monitoring cantilever deflection caused by the heat exchanged between them [32-34]. Researchers have also used bi-material microcantilevers with integrated heaters to store high-density data [35, 36], take topographical images [37], and detect vapour [38]. In addition to the aforementioned applications, Glenn et al. have demonstrated photothermal heating of bi-material cantilevers using a modulated laser source for tapping-mode of AFM in liquids in order to simplify solution imaging [39]. In regard to all

applications discussed above, having a deep knowledge of a microcantilever's heat transfer is absolutely imperative.

In this study, we have focused on the heat transfer of bi-material cantilevers used in a PCDS setup and the effect of convection heat transfer on thermal sensitivity of bi-material cantilevers. An experiment methodology is presented in order to measure the effective convection heat transfer coefficient (*h)* of bi-material cantilevers at room temperature. The *h* values were experimentally determined using the same cantilevers discussed within the previous PCDS section.

5.1.2 Available heat transfer models

5.1.2.1 Models without convection heat loss term

The first theoretical models of temperature distribution for microcantilevers due to power absorbed by the cantilever surface were proposed by Gerber et al. [18]. Since cantilever deflection is a function of cantilever temperature distribution (as shown in equation(3.3)), they presented a few simple heat transfer models for a bi-material cantilever used as a calorimeter where the bi-material cantilevers were assumed to be a perfect heat sink, and heat loss by convection mechanism to the surrounding is negligible [18]. In the following paragraphs, these models will be discussed.

The deflection of bi-material cantilevers is calculated by solving the differential equation (3.3) based on Euler-Bernoulli beam theory [40]:

$$\frac{d^2z}{dx^2} = 6(a_1 - a_2)\left(\frac{t_1 + t_2}{t_2^{\,2}K}\right)[T(x) - T_0] \tag{3.3}$$

where

$$K = 4 + 6(\frac{t_1}{t_2}) + 4(\frac{t_1}{t_2})^2 + \left(\frac{E_1}{E_2}\right)(\frac{t_1}{t_2})^3 + \left(\frac{E_2}{E_1}\right)(\frac{t_2}{t_1}) \quad (3.4)$$

α is the thermal expansion coefficient, t is the thickness of layers, *T(x)* is the temperature distribution along the cantilever beam , T_0 is the original cantilever temperature at zero deflection point, *z* is the deflection of the cantilever at the point *x* along the cantilever beam. The subscripts 1 and 2 correspond to the two different cantilever materials.

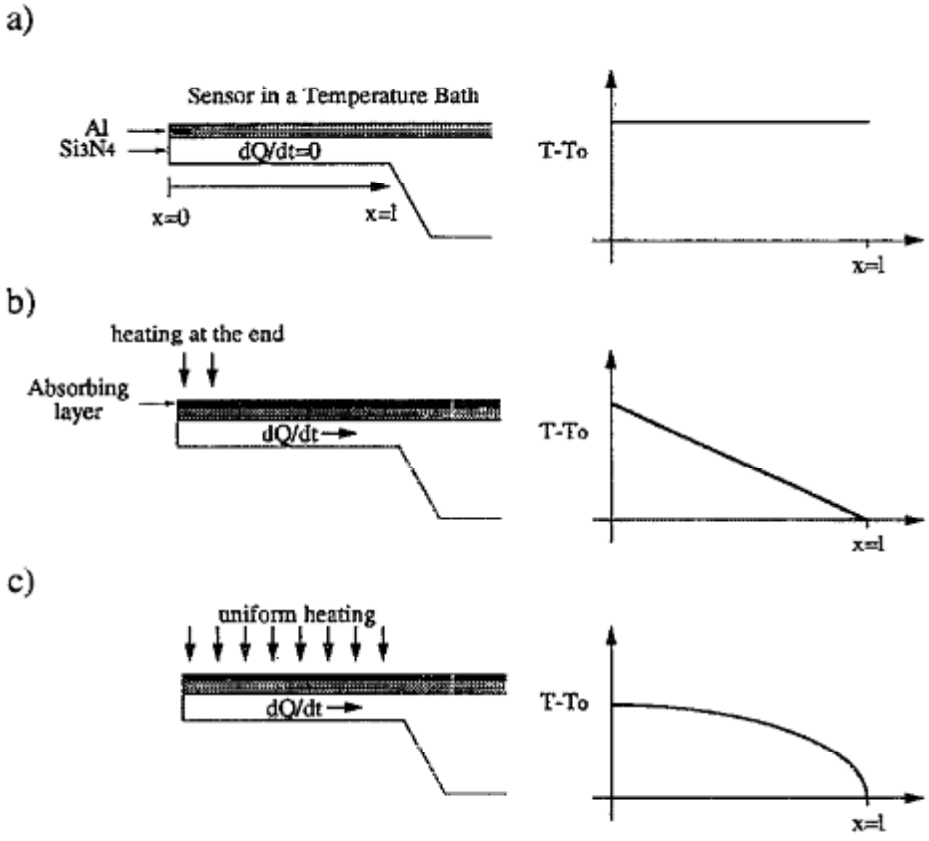

Figure 5.1. Three different models of heat transfer mechanisms and temperature distributions. a) A uniform temperature distribution is assumed. b) Heat is assumed to radiate only at the end of the cantilever. c) The cantilever bends as a result of a uniform heating source. In all cases heat loss to the surrounding is considered negligible [18].

Figure 5.1 (a) shows temperature profiles along a cantilever when the temperature along the cantilever is constant. In Figure 5.1 (b) heat is absorbed only at its free end and heat convection loss is negligible, while in Figure 5.1 (c) heat is absorbed uniformly along the cantilever length. The obtained temperature distribution functions for these last two cases are shown in equation(3.5) and equation(3.6), respectively.

$$T(x) - T_0 = (l - x)\frac{P}{w(l_1 t_1 + l_2 t_2)} \tag{3.5}$$

$$T(x) - T_0 = (l^2 - x^2)\frac{P}{2lw(l_1 t_1 + l_2 t_2)} \tag{3.6}$$

Here, P is the incident power on the microcantilever, l and w is the length and width of the cantilever beam, respectively, and λ is the thermal conductivity of bi-material cantilever layers [18]. These model's lack of sufficient accuracy has led researchers to propose more complicated models that consider heat dissipated by the convection heat transfer mechanism [41-45].

5.1.2.2 Models with convection heat loss

Given that in most applications bi-material cantilevers operate in an air environment, neglecting convection heat loss from cantilever to air might impair the models' accuracy [41]. Recently, King at al. have presented a new model for thermal sensitivity of bi-material cantilevers in the mid-IR spectral region [44]. Their model is based on temperature distribution considering convection heat transfer of microcantilevers. They demonstrated how the convection heat transfer coefficient (*h)* affects the cantilever thermal

sensitivity and even the optimum thickness ratio (the ratio which yields maximum deflection) of bi-material cantilevers. Therefore, designing an experiment for measuring the convection heat transfer coefficient (h), prior to any PCDS experiment, seems vital to reach the maximum thermal sensitivity of microcantilever sensors [44].

Here, the physics based model proposed by King is discussed in detail. Some simplifications are required in order to achieve a theoretical model. Firstly, the incident IR light is assumed to heat the bi-material cantilever surface uniformly. Secondly, the temperature distribution in the cantilever varies only along the beam length since the cantilever thickness is very small compared to its length. Another assumption is that heat losses to the surrounding air are due to the conduction heat transfer mechanism which will be discussed later. The effective heat transfer coefficient is estimated as h = 1000 W/m^2.K [46-48]. The temperature profile T(x) along the cantilever length, considering all above assumptions and appropriate boundary conditions, is shown in equation (3.7) [44].

$$T(x)-T_0=\frac{P}{2hL(t_1+t_2+w)} \times\left[\tanh(bL)\sinh(bx)-\cosh(bx)+1\right] \tag{3.7}$$

where

$$b=\sqrt{\frac{2(t_1+t_2+w)h}{(l_1t_1+l_2t_2)w}} \tag{3.8}$$

Here, L is cantilever length, w is cantilever width, λ is the thermal conductivity of the cantilever, and P is the absorbed incident IR light on the cantilever

surface. The subscripts 1 and 2 correspond to the two different cantilever materials. Substituting $T(x)$ into equation (3.3) yields the following analytical solution of the cantilever deflection:

$$z(L) = 3(a_1 - a_2)\left(\frac{t_1 + t_2}{t_2^{\,2} K}\right)\frac{P}{hLb^{\,2}(t_1 + t_2 + w)} \times\left[\tanh(bL)\sinh(bL) - \cosh(bL) + \frac{1}{2}b^{\,2}L^2 + 1\right] \tag{3.9}$$

The thermal sensitivity of a bi-material cantilever irradiated by mid-infrared light is defined as angular displacement per unit of absorbed power [44]. Thus,

$$S = \frac{1}{P}.\frac{dz}{dx}_{x=L} = 3(a_1 - a_2)\left(\frac{t_1 + t_2}{t_2^{\,2} K}\right)\frac{1}{hL(t_1 + t_2 + w)}\left(L - \frac{\tanh(bL)}{b}\right) \tag{3.10}$$

Though the above analytical calculations have proposed the most accurate model so far, lack of broad knowledge of the effective convection heat transfer coefficient (h) around micro-sized machined structures is a major source of error.

A significant point about the equation (3.10) (not mentioned by King [44]) is that the thermal sensitivity of bi-material cantilevers in mid-infrared spectroscopy surprisingly depends on the effective convection heat transfer coefficient (h) as is shown in Figure 5.2. As h increases, the thermal sensitivity of bi-material cantilever decreases since more heat stored in the cantilever is transferred to the surrounding air which in turn results in less cantilever bending. In addition to this effect of h on the bi-material cantilever thermal sensitivity, the optimum thickness ratio of bi-material cantilever changes with different h are shown in Table 1. Therefore, in the PCDS experiments, greater thermal sensitivity would be achieved by reducing the effective convection

heat transfer coefficient (*h*). In addition, a more thinly applied gold layer is needed which would in turn simplify the cantilever coating process.

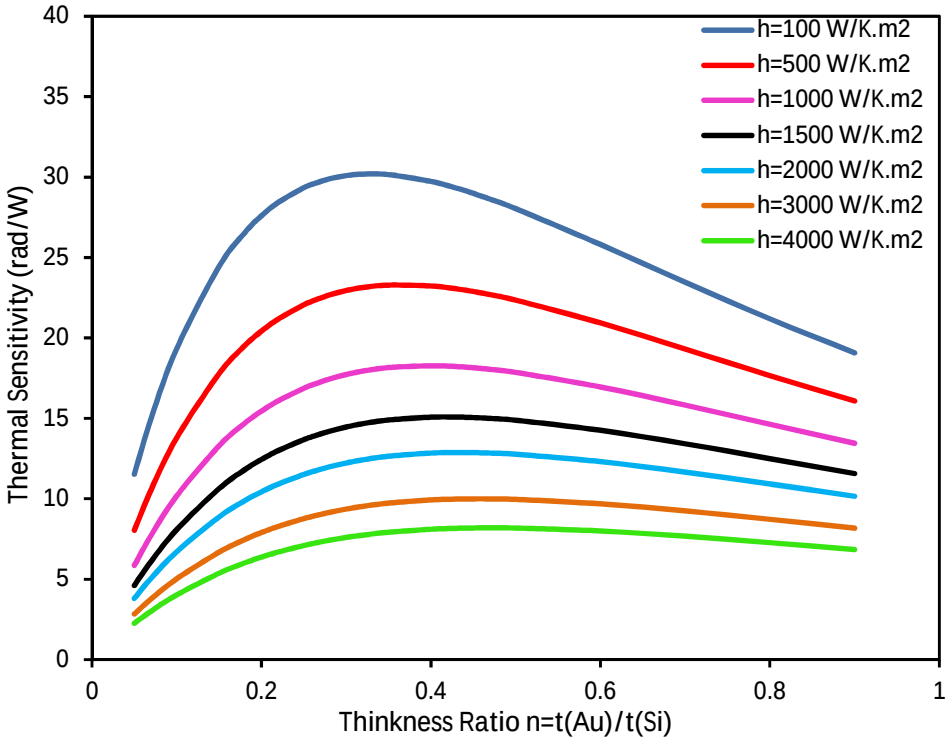

Figure 5.2. The effective convection heat transfer coefficient (*h*) effect on the thermal sensitivity of the bi-material microcantilever in a PCDS setup.

Effective convection heat transfer coefficient h(W/K.m^2)	The optimum thickness ratio of Gold and Silicon
100	0.32
500	0.35
1000	0.40
1500	0.41
2000	0.43
3000	0.45
4000	0.47

Table 1. The optimum thickness ratio of the bi-material cantilever (Gold and Silicon) in a PCDS setup as a function of different estimated *h* values.

5.1.2.3 Convection term

Convection heat transfer takes place whenever a fluid is in contact with a solid surface which is at a different temperature the fluid. When a driving force moves a fluid past a surface, it is called forced convection. If fluid motion is due to a density difference caused by a temperature gradient in the fluid, then it is called natural convection. Several theoretical and empirical models have been suggested for both forced and natural convection in various conditions. In macro-sized structures, the natural convection heat transfer coefficient (*h*) can be estimated using free convection correlation equations based on the Rayleigh number as shown in equation (3.11) [49].

$$Ra = \frac{g.b}{n.a}\Delta T.L^3 \qquad (3.11)$$

Where g is gravity constant, β is thermal expansion coefficient, L is characteristic length, ΔT is temperature difference between surface and fluid, $v = \eta/\rho$ (viscosity/density) is kinematic viscosity, and α is thermal diffusivity.

In spite of macroscale, these correlations are not valid for micro-sized structures such as microcantilevers since their Rayleigh numbers are too small. The Rayleigh number is a dimensionless number defined in natural convection which indicates either conduction or convection as a predominant heat transfer mechanism. In microcantilever case, the Rayleigh number is of the order of 10^{-5}. If the Rayleigh number is smaller than 1700 (i.e. critical value), then heat loss from cantilevers to the surrounding air is mostly transferred by conduction mechanism. This energy loss is still termed convection and an effective convection coefficient is defined, not to be confused with conduction inside the cantilever [41, 49].

6 Experimental setup and experiments

The experiments were carried out using five commercially available silicon microcantilevers (OCTOSENSIS-Micromotive GmbH, Germany). The cantilever chips contain an array of eight cantilevers having typical dimensions of 500 µm in length, 90 µm in width, and 1.0 ± 0.3µm in thickness with a spring constant of 23 mN/m and corresponding resonance frequency of 24.3 KHz. The microcantilevers were coated with 50, 100, 150, 200 nm gold layer and 10 nm Ti as an adhesion layer using an e-beam evaporator. Prior to each coating process, microcantilever resonance frequencies were measured to select microcantilevers with identical physical properties.

The cantilevers were then mounted on a thin aluminum holder of a heater which controlled the temperature using a programmable temperature controller (Hanyoung, Inchon, Korea). The heater surface, as shown in Figure 6.1, was only in contact with the cantilever base while the heater surface in contact with the surrounding air was sealed in order to prevent the air temperature (T_∞) rise. A thermocouple was positioned close to the experimental setup in order to monitor the surrounding air temperature. The temperature was cycled from 25 ^oC to approximately 60 ^oC several times to increase the accuracy of the experiment. The heating and cooling rates were maintained at 10 ^oC/min.

The temperature-dependent changes in the deflections of the cantilevers were measured as a function of the cantilever base temperature

(T_b) which is assumed equal with the heater temperature. During the temperature cycling, a focused laser beam was reflected off the free end of the cantilever onto a duo-lateral position-sensitive detector (SiTek Electro Optics, Partille, Sweden). The absolute deflection values of the cantilevers were calibrated using a piece of silicon with a 25 nm level aluminium-coated layer.

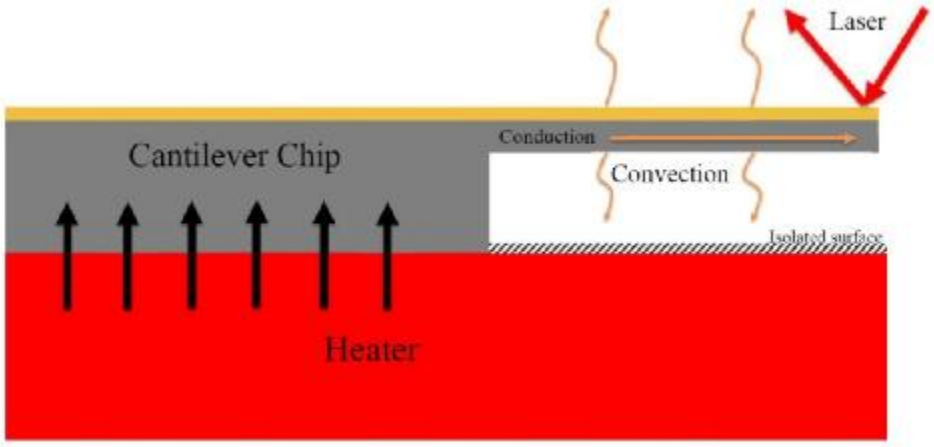

Figure 6.1. Schematic of experimental apparatus to measure thermal responses of bi-material cantilevers. A controllable heater changes the cantilever base temperature and the resulting bending of cantilever is monitored by the laser reflected off the cantilever to the PDS. A thermocouple (not shown in the figure) is positioned close to the air around the cantilever to monitor ambient temperature T_∞.

7 Result and discussion

Lack of consistent data for the convection heat transfer coefficient (h) has hindered a comprehensive study of heat transfer. Though a few papers recently have reported some (h) values for microcantilevers, a considerable discrepancy identified between reported values practically discredits the results for other researches. The discrepancy might originate from many factors such as differences in micro-structure geometries, ambient air conditions (i.e. temperature, humidity), assumptions, and systematic error of experiments.

Due to the previously mentioned reasons, in this chapter we present a simple experiment to measure (h) under the identical experimental conditions in which our PCDS experiments were carried out. First, a heat transfer model for the microcantilevers will be developed and then, in the second part, the experimental results will be discussed.

7.1.1 Theory

For the temperature profile analysis, an arbitrary control volume of the cantilever is taken. Energy conservation applied to the control volume can be expressed as,

$$Q_{in} - Q_{out} = 0 \tag{3.12}$$

$$-l\,A\frac{dT}{dx}_{x} + l\,A\frac{dT}{dx}_{x+\Delta x} - hA'(T - T_{\infty}) = 0 \tag{3.13}$$

Here, A is the cross section of cantilever area perpendicular to the conduction heat transfer and A' is the surface area around the cantilever where heat is dissipated to the surrounding medium as shown in equation(3.13). λ is the thermal conductivity of the cantilever, h is effective convection heat transfer, and T_∞ is temperature of air around the cantilever. Using Fourier's law gives

$$\frac{d^2q}{dx^2} - m^2q = 0 \tag{3.14}$$

where

$$m^2 = \frac{2h}{l_1t_1 + l_2t_2} \tag{3.15}$$

and

$$q = T(x) - T_\infty \tag{3.16}$$

The subscripts 1 and 2 correspond to the two different cantilever materials. The analytical solution of the equation (3.14) can be solved as

$$q(x) = C_1e^{mx} + C_2e^{-mx} \tag{3.17}$$

Equation(3.14) needs two boundary conditions given by equation (3.18) and (3.19). At the base of the cantilever (x = L), temperature is the cantilever base temperature T_b which is a known parameter in this experiment.

$$q(L) = T_b - T_\infty \tag{3.18}$$

At the free end of the cantilever ($x = 0$), P is the incident laser power absorbed by the cantilever. Thus,

$$\frac{dq(0)}{dx} = -\frac{P}{(l_1 t_1 + l_2 t_2)w} = -G \tag{3.19}$$

Using these two boundary conditions, C_1 and C_2 can be solved as

$$C_1 = \frac{(T_b - T_\infty) - \frac{G}{m}e^{-mL}}{e^{mL} + e^{-mL}}$$

$$C_2 = \frac{(T_b - T_\infty) - \frac{G}{m}e^{mL}}{e^{mL} + e^{-mL}}$$

Substituting C_1 and C_2 in equation (3.17) and rearranging gives the temperature distribution as

$$q(x) = T(x) - T_\infty = \frac{(T_b - T_\infty) - \frac{G}{m}e^{-mL}}{e^{mL} + e^{-mL}}e^{mx} + \frac{(T_b - T_\infty) - \frac{G}{m}e^{mL}}{e^{mL} + e^{-mL}}e^{-mx} \tag{3.20}$$

With T(x) - T_0 obtained from equation (3.17), equation (3.3) can be rewritten as

$$z(x) = b\left(\frac{(T_b - T_\infty) - \frac{G}{m}e^{-mL}}{e^{mL} + e^{-mL}} \times \frac{e^{mx}}{m^2} + \frac{(T_b - T_\infty) - \frac{G}{m}e^{mL}}{e^{mL} + e^{-mL}} \times \frac{e^{-mx}}{m^2}\right) + A_1 x + A_2 \tag{3.21}$$

where

$$b = 6(a_1 - a_2)\left(\frac{t_1 + t_2}{t_2{}^2 K}\right)$$

Because both the deflection and the slope at the base of cantilever (x = 0) are 0, unknown constants A_1 and A_2 can be expressed as

$$A_1 = -b\left(C_2 \frac{e^{-ml}}{m} - C_1 \frac{e^{ml}}{m}\right)$$

$$A_2 = -b\left(C_1\frac{e^{ml}}{m^2} + C_2\frac{e^{-ml}}{m^2}\right) - A_1 L$$

Then using equation(3.21), the analytical solution for cantilever deflection at the free end can be readily predicted via equation (3.22)

$$z(0) = b\left(C_1\frac{1}{m^2} + C_2\frac{1}{m^2}\right) + A_2 \tag{3.22}$$

The derivative of z(0) with respect to T_b are shown in the equation (3.23).

$$\frac{dz(0)}{dT_b} = \frac{b}{m^2}\left[\frac{1}{\cosh(mL)} - 1 - mL\right] \tag{3.23}$$

By using equation(3.23) and measuring the derivative of z(0) with respect to T_b from the experimental results, m will be determined. Consequently, we can calculate h using equation(3.15).

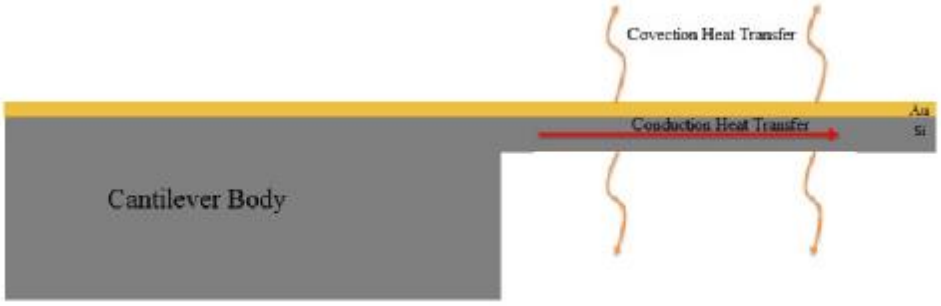

Figure 7.1. The heat transfer of a bi-material cantilever. There are two heat transfer mechanisms: first, conduction of heat inside the cantilever. Second, convection of heat to air around the cantilever by conduction mechanism.

7.1.2 Experiment

There are various possible factors that might affect the accuracy of the experimental measurements of the h value in the microscale [46, 50, 51]. Firstly, in experiments using a laser as a heating source [51], measuring the absorbed laser power would be challenging and a source of error. Secondly, non-insulated heaters causing the surrounding air temperature rise (T_∞) might impair the measurement's accuracy. To mitigate these potential sources of error, the model used is independent of laser power and the heater surface was insulated to significantly diminish thermal variance of the surrounding air in the experiments.

Using our experimental setup as shown in Figure 6.1, the deflections of all cantilevers as a function of T_b were measured. Figure 7.2 shows the deflections of a cantilever coated with 50 nm gold. The values for the effective convection heat transfer coefficients (h) were calculated by using equation(3.23), (3.15), and the slope obtained from Figure 7.3 . The h was calculated for the five 50 nm gold-coated microcantilever chips having similar resonance frequencies. Figure 7.3 displays the calculated h values obtained from these 5 measurements. The results for h given by different chip's experiments exhibit a high concurrence with only slight deviation.

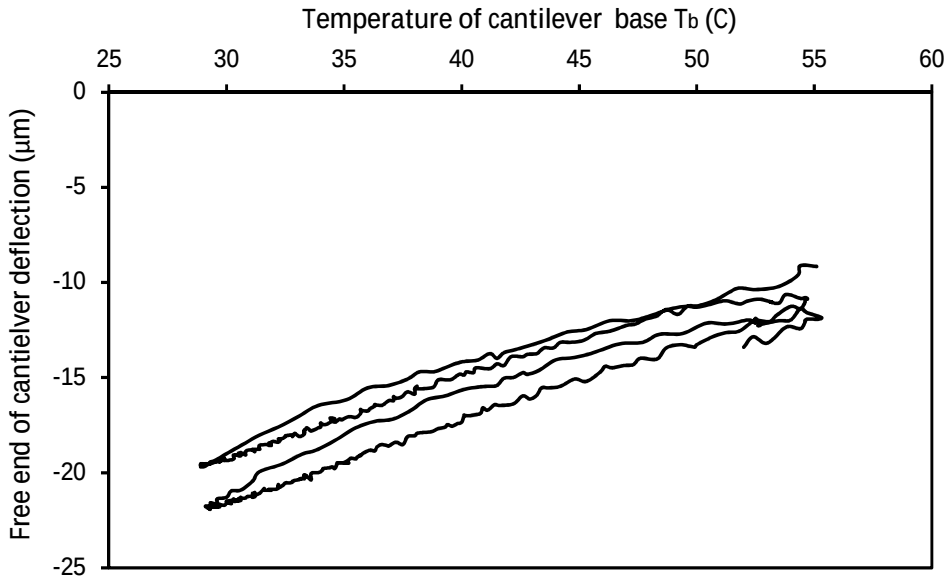

Figure 7.2. The variation of bi-material cantilever tip deflection for 50 nm gold-coated cantilever with the cantilever base temperature cycling.

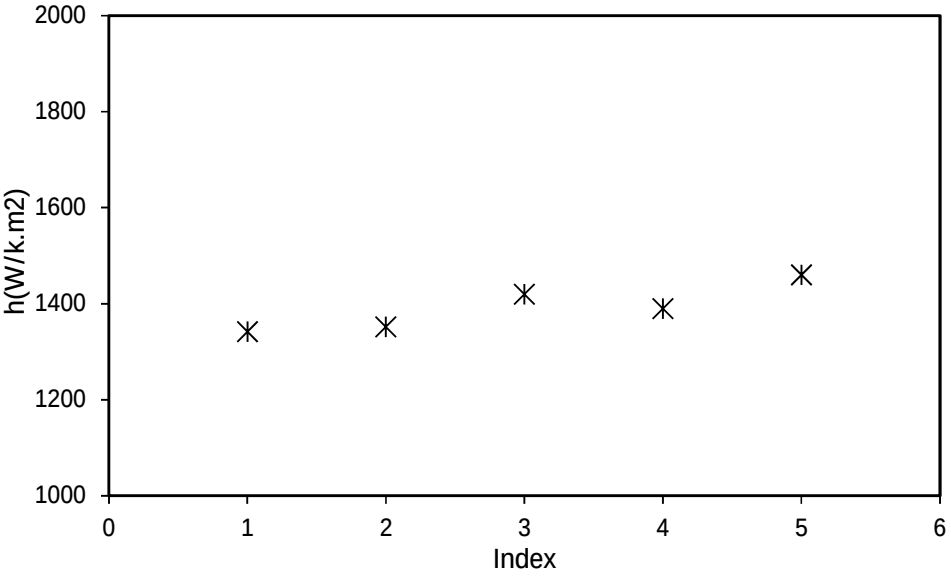

Figure 7.3. The effective convection heat transfer of the five 50 nm gold-coated microcantilevers. The obtained results for *h* show only slight difference.

Figure 7.4 to Figure **7.9** also illustrate the same results for 100, 150, 200 nm gold-coated microcantilevers, respectively. After each measurement,

these five bi-material cantilevers were cleaned by the method disclosed in section 2.1 and coated with an additional 50 nm gold layer.

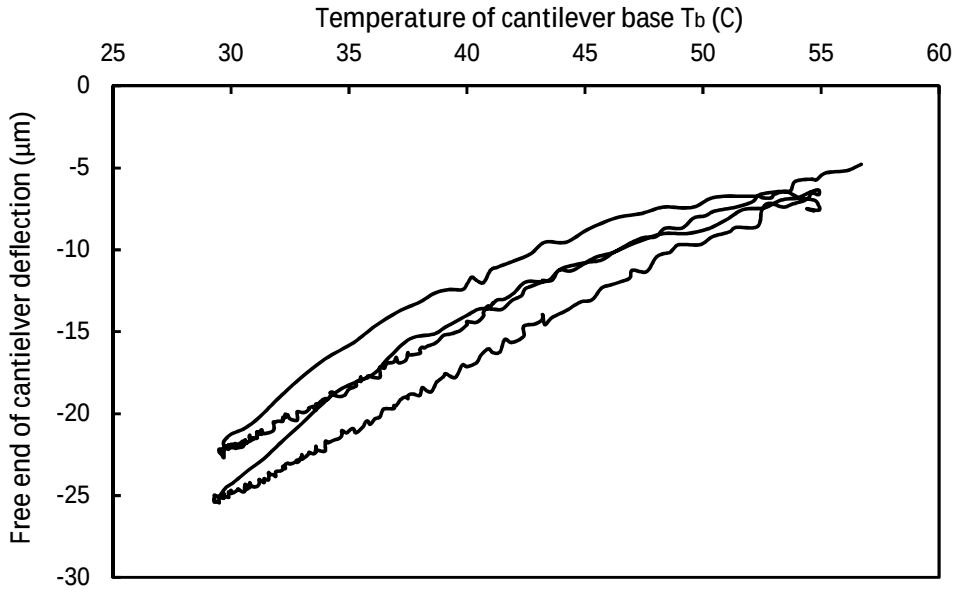

Figure 7.4. The variation of bi-material cantilever tip deflection for 100 nm gold-coated cantilever with the cantilever base temperature cycling.

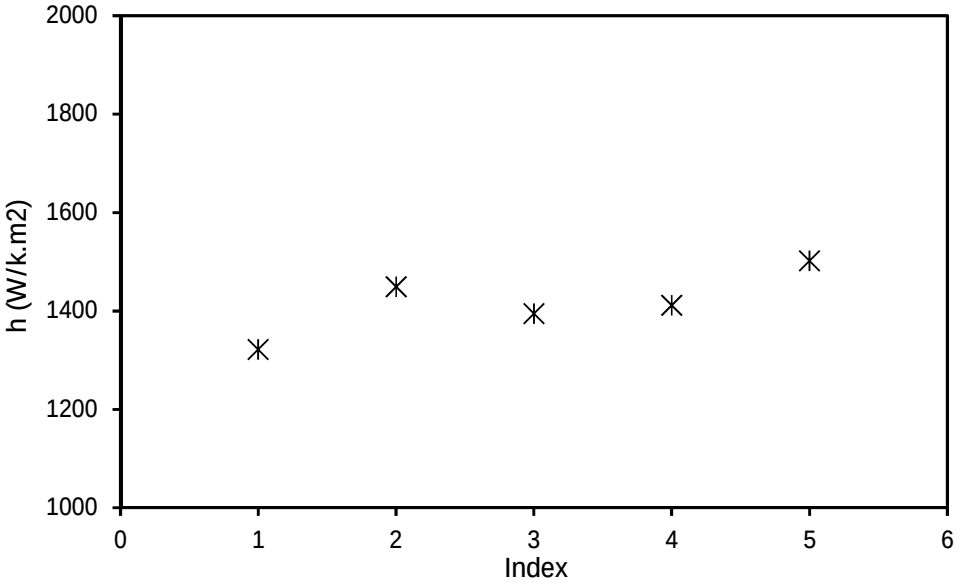

Figure 7.5. The effective convection heat transfer of the five 100 nm gold-coated microcantilevers.

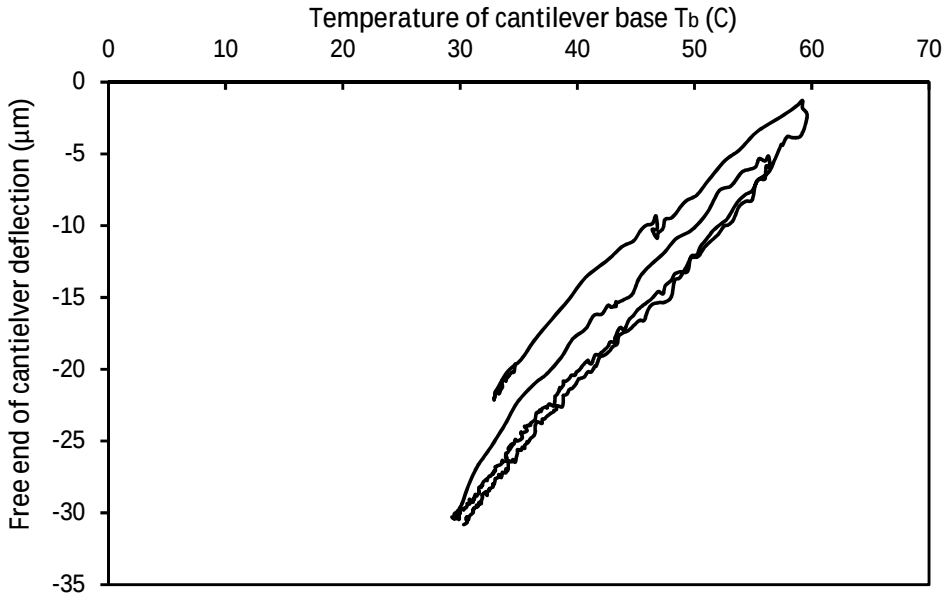

Figure 7.6. The variation of bi-material cantilever tip deflection for 150 nm gold-coated cantilever with the cantilever base temperature cycling.

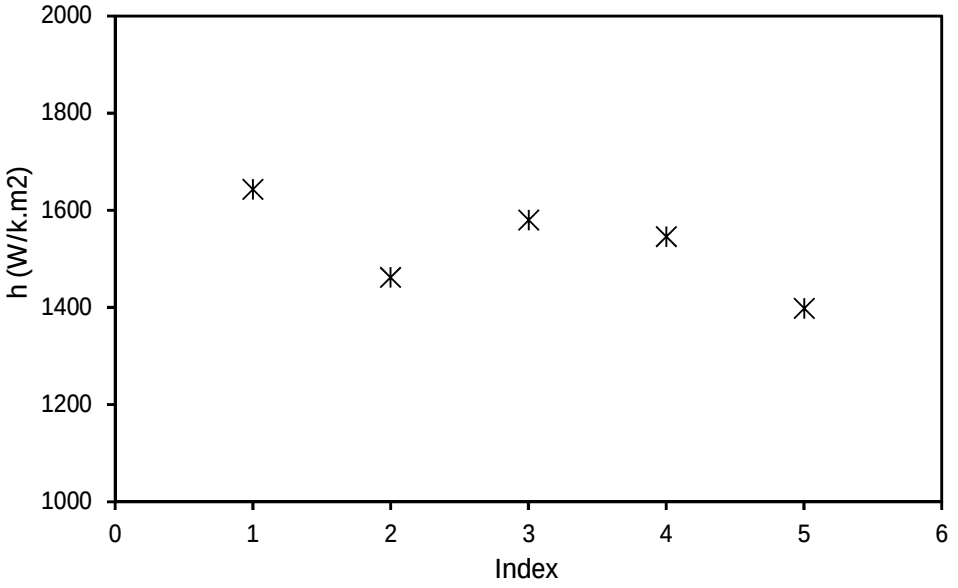

Figure 7.7. The effective convection heat transfer of the five 150 nm gold-coated microcantilevers.

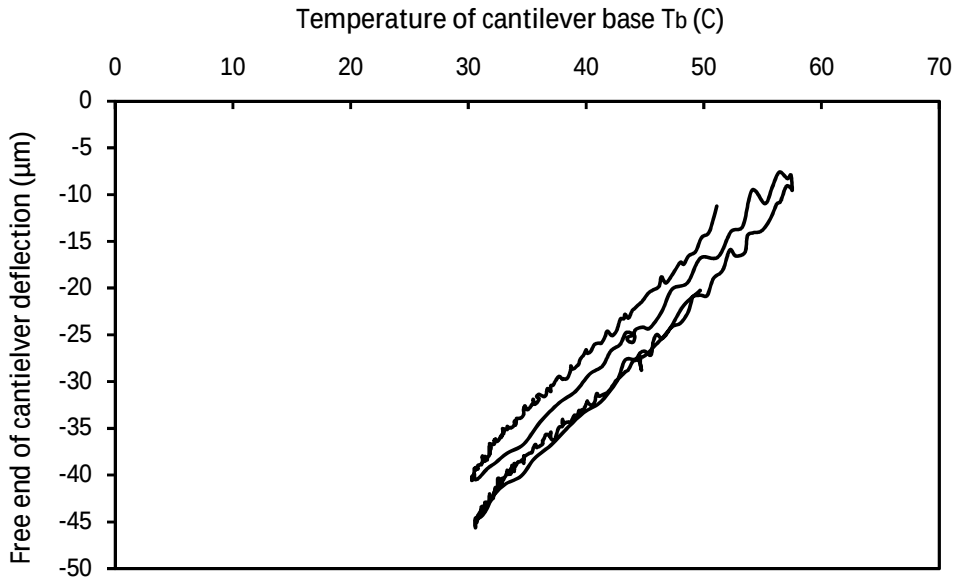

Figure 7.8. The variation of bi-material cantilever tip deflection for 200 nm gold-coated cantilever with the cantilever base temperature cycling.

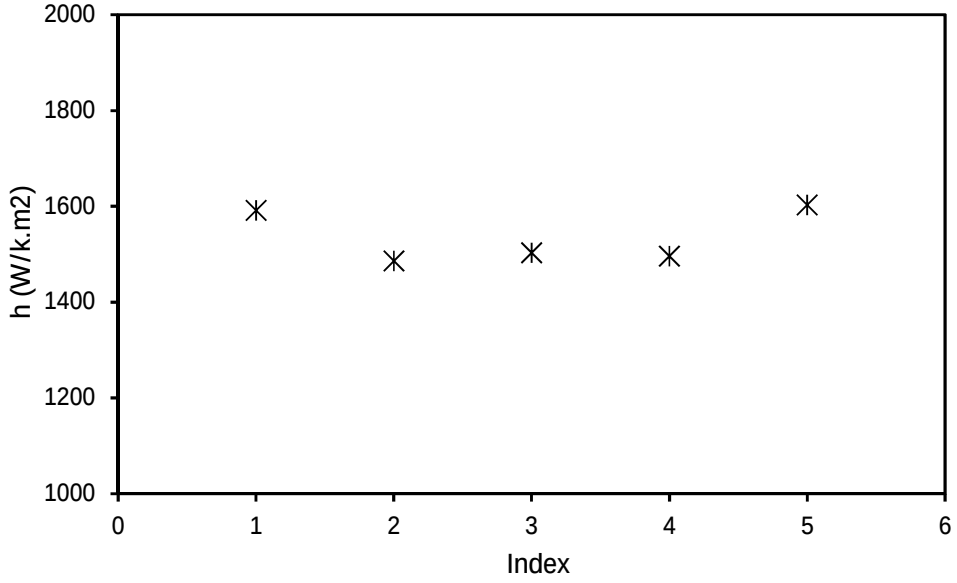

Figure 7.9. The effective convection heat transfer of the five 200 nm gold-coated microcantilevers.

Regarding the above results, the obtained h values for the five cantilever chips coated with different thicknesses of gold layers with a slight variation have the same values which in turn validate our results. The h value has been estimated 1350-1650 W/K.m^2 for the microcantilevers used in this study. However, a wide range of h can be found in published literature usually ranging from 500 to 4000 W/K.m^2, the attained result in this study is in a reasonable value and it is confirmed by previous works [41, 44, 47]. Using an estimation for h based on spreading resistance for an isoflux heat transfer between a cantilever and ambient air results to h≈580 W/K.m^2 [51]. The isoflux heat transfer assumption might be a reason for the discrepancy between estimated and measured h values. In addition, due to the small size of the cantilever, humidity should be taken into account since it might increase the thermal conductivity of air significantly.

The designed experiment for measuring h values of microcantilevers helps us to have a broader knowledge about the heat transfer of cantilevers in PCDS experiments. As previously mentioned, variation in h value can affect both the thermal sensitivity and optimum thickness ratio of bi-material cantilevers exposed to mid-infrared light. Therefore, the thermal sensitivity and optimum thickness ratio prediction is possible for PCDS setups with a known effective convection heat transfer. Besides the ways discussed in the section 4 to improve the PCDS detection capability (which is the main goal of this study), modification of h by changing surrounding air temperature can also be an alternative.

8 Conclusion

In conclusion, we pointed out that the effective convection heat transfer coefficient (h) affects the thermal sensitivity and the optimum thickness ratio of the bi-material microcantilevers used in a PCDS setup. Due to the lack of precise data for h of air surrounding cantilevers, we developed an experiment and a model corresponded to heat transfer of a bi-material cantilever to determine the h value. The h that was obtained by using our straightforward technique is 1350-1650 $W/k.m^2$. The experiments were repeated for the five bi-material cantilevers with different gold thickness to reach more reliable data.

9 Future Work

Future works are focused on two aspects. Frist is increasing sensor sensitivity by using different kind of cantilever sensors like AAO (Anodic aluminium oxide) cantilevers having more capacity for adsorbing naphtha. Second is designing a microfluidic platform to pre-concentrate the tailing samples and remove solid particles. In addition, this platform makes a mico-droplet of sample fluid with specific volume to deposit it on the cantilever sensor surface.

Reference

[1] Perry R H G, D.W 1997 *Perry's Chemical Engineers' Handbook* (New York: McGraw-Hill)

[2] Humphries M 2009 North American Oil Sands: History of Development, Prospects for the Future *Energy Research Developments: Tidal Energy, Energy Efficiency and Solar Energy* 287-311

[3] Rajasekar A, Maruthamuthu S, Muthukumar N, Mohanan S, Subramanian P and Palaniswamy N 2005 Bacterial degradation of naphtha and its influence on corrosion *Corros Sci* **47** 257-71

[4] Binnig G, Quate C F and Gerber C 1986 Atomic force microscope *Physical review letters* **56** 930-3

[5] Wolter O, Bayer T and Greschner J 1991 Micromachined Silicon Sensors for Scanning Force Microscopy *J Vac Sci Technol B* **9** 1353-7

[6] Madou M J 2002 *Fundamentals of microfabrication : the science of miniaturization* (Boca Raton: CRC Press)

[7] Thundat T, Warmack R J, Chen G Y and Allison D P 1994 Thermal and Ambient-Induced Deflections of Scanning Force Microscope Cantilevers *Appl Phys Lett* **64** 2894-6

[8] Chen G Y, Thundat T, Wachter E A and Warmack R J 1995 Adsorption-Induced Surface Stress and Its Effects on Resonance Frequency of Microcantilevers *J Appl Phys* **77** 3618-22

[9] Thundat T, Wachter E A, Sharp S L and Warmack R J 1995 Detection of Mercury-Vapor Using Resonating Microcantilevers *Appl Phys Lett* **66** 1695-7

[10] Boisen A, Dohn S, Keller S S, Schmid S and Tenje M 2011 Cantilever-like micromechanical sensors *Reports on Progress in Physics* **74**

[11] Raiteri R, Grattarlo M, Butt H, J. and Skládal P 2001 Micromechanical cantilever-based biosensors *Sensors and Actuators B: Chemical* **79** 115-26

[12] Ji H F, Hansen K M, Hu Z and Thundat T 2001 Detection of pH variation using modified microcantilever sensors *Sensor Actuat B-Chem* **72** 233-8

[13] Dauksaite V, Lorentzen M, Besenbacher F and Kjems J 2007 Antibody-based protein detection using piezoresistive cantilever arrays *Nanotechnology* **18**

[14] Lee D, Jin Y, Jung N, Lee J, Lee J, Jeong Y S and Jeon S 2011 Gravimetric Analysis of the Adsorption and Desorption of CO2 on Amine-Functionalized Mesoporous Silica Mounted on a Microcantilever Array *Environ Sci Technol* **45** 5704-9

[15] Zhao Y, Ganapathysubramanian B and Shrotriya P 2012 Cantilever deflection associated with hybridization of monomolecular DNA film *J Appl Phys* **111**

[16] Kang K H, Shrotriya P and Asme 2010 *SURFACE STRESS DEVELOPMENT ASSOCIATED WITH HYBRIDIZATION OF MONOMOLECULAR DNA FILM*

[17] Gimzewski J K, Gerber C, Meyer E and Schlittler R R 1994 Observation of a Chemical-Reaction Using a Micromechanical Sensor *Chem Phys Lett* **217** 589-94

[18] Barnes J R, Stephenson R J, Woodburn C N, Oshea S J, Welland M E, Rayment T, Gimzewski J K and Gerber C 1994 A Femtojoule Calorimeter Using Micromechanical Sensors *Rev Sci Instrum* **65** 3793-8

[19] Barnes J R, Stephenson R J, Welland M E, Gerber C and Gimzewski J K 1994 Photothermal Spectroscopy with Femtojoule Sensitivity Using a Micromechanical Device *Nature* **372** 79-81

[20] Wachter E A, Thundat T, Oden P I, Warmack R J, Datskos P G and Sharp S L 1996 Remote optical detection using microcantilevers *Rev Sci Instrum* **67** 3434-9

[21] Datskos P G, Rajic S, Sepaniak M J, Lavrik N, Tipple C A, Senesac L R and Datskou I 2001 Chemical detection based on adsorption-induced and photoinduced stresses in microelectromechanical systems devices *J Vac Sci Technol B* **19** 1173-9

[22] Krause A R, Van Neste C, Senesac L, Thundat T and Finot E 2008 Trace explosive detection using photothermal deflection spectroscopy *J Appl Phys* **103**

[23] Van Neste C W, Senesac L R, Yi D and Thundat T 2008 Standoff detection of explosive residues using photothermal microcantilevers *Appl Phys Lett* **92**

[24] Fadini A and Schnepel F M 1989 *Vibrational spectroscopy : methods and applications* (Chichester New York: E. Horwood ; Halsted Press)

[25] Lai J, Perazzo T, Shi Z and Majumdar A 1997 Optimization and performance of high-resolution micro-optomechanical thermal sensors *Sensor Actuat a-Phys* **58** 113-9

[26] Stuart B H 2004 *Infrared Spectroscopy: Fundamentals and Applications* (England: Wiley)

[27] Schrader B and Bougeard D 1995 *Infrared and Raman spectroscopy : methods and applications* (Weinheim ; New York: VCH)

[28] Minhyuk Yun S K, Dongkyu Lee, Namchul Jung, Inseok Chae, Sangmin Jeon, Thomas Thundat 2012 Photothermal cantilever deflection spectroscopy of a photosensitive polymer *Appl Phys Lett* **100** 4

[29] Wig A, Arakawa E T, Passian A, Ferrell T L and Thundat T 2006 Photothermal spectroscopy of Bacillus anthracis and Bacillus cereus with microcantilevers *Sensor Actuat B-Chem* **114** 206-11

[30] Min-Sik Ku H C 1999 Compositional Analysis of Naphtha by FT-Raman Spectroscopy *Korean Chemical Society* **20** 159-62

[31] Li G M, Burggraf L W and Baker W P 2000 Photothermal spectroscopy using multilayer cantilever for chemical detection *Appl Phys Lett* **76** 1122-4

[32] Narayanaswamy A, Shen S and Chen G 2008 Near-field radiative heat transfer between a sphere and a substrate *Phys Rev B* **78**

[33] Rousseau E, Siria A, Jourdan G, Volz S, Comin F, Chevrier J and Greffet J J 2009 Radiative heat transfer at the nanoscale *Nat Photonics* **3** 514-7

[34] Shen S, Narayanaswamy A and Chen G 2009 Surface Phonon Polaritons Mediated Energy Transfer between Nanoscale Gaps *Nano letters* **9** 2909-13

[35] Binnig G, Despont M, Drechsler U, Haberle W, Lutwyche M, Vettiger P, Mamin H J, Chui B W and Kenny T W 1999 Ultrahigh-density atomic force microscopy data storage with erase capability *Appl Phys Lett* **74** 1329-31

[36] Vettiger P, Cross G, Despont M, Drechsler U, Durig U, Gotsmann B, Haberle W, Lantz M A, Rothuizen H E, Stutz R and Binnig G K 2002 The "millipede" - Nanotechnology entering data storage *Ieee T Nanotechnol* **1** 39-55

[37] Kim S J, Ono T and Esashi M 2009 Thermal imaging with tapping mode using a bimetal oscillator formed at the end of a cantilever *Rev Sci Instrum* **80**

[38] Pinnaduwage L A, Gehl A, Hedden D L, Muralidharan G, Thundat T, Lareau R T, Sulchek T, Manning L, Rogers B, Jones M and Adams J D 2003 A microsensor for trinitrotoluene vapour *Nature* **425** 474-

[39] Ratcliff G C, Superfine R and Erie D A 1998 Photothermal modulation for oscillating mode atomic force microscopy in solution *Biophysical journal* **74** A187-A

[40] Roark R J and Young W C 1975 *Formulas for stress and strain* (New York: McGraw-Hill)

[41] Toda M, Ono T, Liu F and Voiculescu I 2010 Evaluation of bimaterial cantilever beam for heat sensing at atmospheric pressure *Rev Sci Instrum* **81**

[42] Mahmoud S, Al-Dadah R, Aspinwall D K, Soo S L and Hemida H 2011 Effect of micro fin geometry on natural convection heat transfer of horizontal microstructures *Appl. Therm. Eng.* **31** 627-33

[43] Hu X J, Jain A and Goodson K E 2008 Investigation of the natural convection boundary condition in microfabricated structures *Int. J. Therm. Sci.* **47** 820-4

[44] Kwon B, Wang C, Park K, Bhargava R and King W P 2011 THERMOMECHANICAL SENSITIVITY OF MICROCANTILEVERS IN THE MID-INFRARED SPECTRAL REGION *Nanoscale and Microscale Thermophysical Engineering* **15** 16-27

[45] Shen S, Narayanaswamya A, Goh S and Chen G 2008 Thermal conductance of bimaterial microcantilevers *Appl Phys Lett* **92**

[46] Kim K J and King W P 2009 Thermal conduction between a heated microcantilever and a surrounding air environment *Appl. Therm. Eng.* **29** 1631-41

[47] Lee J, Wright T L, Abel M R, Sunden E O, Marchenkov A, Graham S and King W P 2007 Thermal conduction from microcantilever heaters in partial vacuum *J Appl Phys* **101**

[48] Park K, Lee J, Zhang Z M and King W P 2007 Frequency-dependent electrical and thermal response of heated atomic force microscope cantilevers *Journal of Microelectromechanical Systems* **16** 213-22

[49] Incropera F P, DeWitt D P, Bergman T L and Lavine A S 2006 *Fundamentals of Heat and Mass Transfer* (Hoboken: Wiley)

[50] Yoshikawa S, Murata R, Shida S, Uwai K, Suzuki T, Katsumata S and Takeshita M 2010 Evaluation of correlation between dissolution rates of loxoprofen tablets and their surface morphology observed by scanning electron microscope and atomic force microscope *Chemical & pharmaceutical bulletin* **58** 34-7

[51] Narayanaswamy A and Gu N 2011 Heat Transfer From Freely Suspended Bimaterial Microcantilevers *Journal of Heat Transfer-Transactions of the Asme* **133**

Appendix I MATLAB Code

```
%%%%%%%%%%%%%%%%%%%%%%%%%%%%%%%%%%%%%%%%%%%%%%%%%%%%%%%%%%%%%%%%%%%%%%%%%%%%
%%   Thermal sensitivity of bi-material cantilever as a function  %%
%%       of cantilever thickness ratio without heat loss term     %%
%%%%%%%%%%%%%%%%%%%%%%%%%%%%%%%%%%%%%%%%%%%%%%%%%%%%%%%%%%%%%%%%%%%%%%%%%%%%

clc
clear
t2=1*10^-6;                  %%%  Cantilever Si layer thickness  %%%
L=500*10^-6;                 %%%       Cantilever length        %%%
w=90*10^-6;                  %%%       Cantilever width         %%%
                          %%% Thermal expansion coefficient of Si %%%
alpha2=ones(20,1)*2.6*10^-6;
                          %%% Thermal expansion coefficient of Au %%%
alpha1=ones(20,1)*14.2*10^-6;
landa2=ones(20,1)*150;       %%%    Thermal conductivity of Si   %%%
landa1=ones(20,1)*296;       %%%    Thermal conductivity of Au   %%%
E2=ones(20,1)*1*10^11;       %%%         Young's modulus of Si   %%%
E1=ones(20,1)*.73*10^11;     %%%         Young's modulus of Au   %%%
gama=landa1./landa2;
n=[.05 .07 .1 .15 .18 .2 .22 .25 .26 .28 .3 .32 .35 .4 .45 .5 .6 .7
.8 .9]';
%%%         n is thickness ration of bi-material cantilever      %%%
%%%                 i.e. n=Au thickness/Si thickness             %%%

K=4+6.*n+4.*n.^2+(E1./E2).*n.^3+(E2./E1)./n;
beta=alpha1./alpha2;
teta=(beta-1).*(n+1)./(K.*(gama.*n+1));

% Thermal sensitivity of bi-material cantilever as a function of n %
S=2.*(alpha2./landa2).*(L.^3/(t2.^2.*w)).*teta;
grid on
plot(n,s)
```

```
%%%%%%%%%%%%%%%%%%%%%%%%%%%%%%%%%%%%%%%%%%%%%%%%%%%%%%%%%%%%%%%%%%%%%%%%%%%%
%%   Thermal sensitivity of bi-material cantilever as a function  %%
%%     of cantilever thickness ratio considering heat loss term   %%
%%%%%%%%%%%%%%%%%%%%%%%%%%%%%%%%%%%%%%%%%%%%%%%%%%%%%%%%%%%%%%%%%%%%%%%%%%%%

clc
clear
ts=1*10^-6;          %%%       Cantilever Si layer thickness      %%%
L=500*10^-6;         %%%            Cantilever length             %%%
w=90*10^-6;          %%%            Cantilever width              %%%
h=100;               %%% effective convection heat transfer Coeff %%%
                     %%%    Thermal expansion coefficient of Si   %%%
alphas=ones(22,1)*2.6*10^-6;
                     %%%    Thermal expansion coefficient of Au   %%%
alphac=ones(22,1)*14.2*10^-6;
landas=ones(22,1)*150;   %%%       Thermal conductivity of Si    %%%
landac=ones(22,1)*296;   %%%       Thermal conductivity of Au    %%%
Es=ones(22,1)*1*10^11;   %%%          Young's modulus of Au      %%%
Ec=ones(22,1)*.73*10^11; %%%          Young's modulus of Si      %%%
gama=landac./landas;
n=[.05 .07 .1 .15 .18 .2 .22 .25 .26 .28 .3 .32 .35 .4 .43 .45 .47
.5 .6 .7 .8 .9]';
%%%         n is thickness ration of bi-material cantilever      %%%
%%%                 i.e. n=Au thickness/Si thickness             %%%

K=4+6./n+4./n.^2+(Es./Ec)./n.^3+(Ec./Es).*n;
beta=((2.*h.*(1+n+w./ts))./((landas+landac.*n).*w)).^0.5;
% Thermal sensitivity of bi-material cantilever as a function of n %

S=-3.*(alphas-
alphac).*((1+n)./(K.*ts.*n.^2)).*(1./(ts.*(1+n+w./ts).*h.*L)).*(L-
(tanh(beta.*L))./beta);
hold on
grid on
plot(n,S)
```